

UNIFIED ONE-DIMENSIONAL SIMULATIONS OF GAMMA-RAY LINE EMISSION FROM TYPE Ia SUPERNOVAE

P. A. MILNE,¹ A. L. HUNGERFORD,² C. L. FRYER, T. M. EVANS, AND T. J. URBATSCH
Los Alamos National Laboratory, P.O. Box 1663, Los Alamos, NM 87545

S. E. BOGGS

Department of Physics, University of California, 366 LeConte Hall, Berkeley, CA 94720

J. ISERN, E. BRAVO, AND A. HIRSCHMANN

Institut d'Estudis Espacials de Catalunya (IEEC), Edifici Nexus, Gran Capita 24, E-08034 Barcelona, Spain

S. KUMAGAI

College of Science and Technology, Nihon University, 101-8308 Tokyo, Japan

P. A. PINTO

Department of Astronomy, University of Arizona, 933 North Cherry Avenue, Tucson, AZ 85721

AND

L.-S. THE

Department of Physics and Astronomy, Clemson University, 118 Kinard Laboratory of Physics, Clemson, SC 29634-1911

Received 2004 April 14; accepted 2004 June 7

ABSTRACT

The light curves of Type Ia supernovae (SNe Ia) are powered by gamma rays emitted by the decay of radioactive elements such as ^{56}Ni and its decay products. These gamma rays are downscattered, absorbed, and eventually reprocessed into the optical emission that makes up the bulk of all SN observations. Detection of the gamma rays that escape the expanding star provide the only direct means to study this power source for SN Ia light curves. Unfortunately, disagreements between calculations for the gamma-ray lines have made it difficult to interpret any gamma-ray observations. Here we present a detailed comparison of the major gamma-ray line transport codes for a series of one-dimensional SN Ia models. Discrepancies in past results were due to errors in the codes, and the corrected versions of the seven different codes yield very similar results. This convergence of the simulation results allows us to infer more reliable information from the current set of gamma-ray observations of SNe Ia. The observations of SN 1986G, SN 1991T, and SN 1998bu are consistent with explosion models based on their classification: subluminous, superluminous, and normally luminous, respectively.

Subject headings: gamma rays: observations — gamma rays: theory — supernovae: general

Online material: color figures

1. INTRODUCTION

Type Ia supernovae (SNe Ia) are intertwined with many of the most interesting frontiers of astrophysics. They occur in all galaxy types and are important contributors to galactic chemical evolution. They are very bright and their peak luminosities are relatively uniform. Furthermore, the variations in peak luminosity that do exist are related to the width of their luminosity peak (hereafter this relation is referred to as the luminosity-width relation, or LWR). This relation has been both calibrated by estimating the distances to the host galaxies of nearby SNe Ia and simulated by performing radiation transport on models purported to span the SN Ia event (Höflich & Khokhlov 1996; Pinto & Eastman 2000a, 2000b). The combination of an extremely bright luminosity peak and the relatively well determined value of that peak (via the empirical LWR) has permitted SNe Ia to be used as high- Z distance indicators. Indeed, SNe Ia have been instrumental in establishing that the Hubble constant (H_0) has a value of $\sim 70 \text{ km s}^{-1}$

Mpc^{-1} (Freedman et al. 2001; Gibson et al. 2000) and in suggesting that the cosmological constant has a nonzero value (Perlmutter et al. 1997; Riess et al. 1998). These uses of SNe Ia proceed despite controversy as to the exact nature of SN Ia explosions.

Studies of the gamma-ray line emission from SNe have long been recognized as a powerful way to probe the nucleosynthesis and explosion kinematics of these events (Clayton et al. 1969; Ambwani & Sutherland 1988; Chan & Lingenfelter 1993). The $^{56}\text{Ni} \rightarrow ^{56}\text{Co} \rightarrow ^{56}\text{Fe}$ decay chain provides the most promising candidates for gamma-ray line studies of prompt emission from SNe, producing strong lines at 158, 812, 847, and 1238 keV. At early times, the line fluxes increase as the expanding ejecta unveils the radio isotopes responsible for each line. The timing of this unveiling is a function of both the distribution of the isotopes and the kinematics of the ejecta. At later times, when the ejecta asymptotically approaches being optically thin to the gamma rays, the line fluxes follow the isotopes' decay curves and reveal the total production of each isotope. Neither of these line flux comparisons requires an instrument capable of resolving the line. If the line can be resolved, measuring the line profiles of the individual lines shows the distribution (in velocity space) of the radio isotopes

¹ Current address: Steward Observatory, University of Arizona, 933 North Cherry Avenue, Tucson, AZ 85721; pmilne@as.arizona.edu.

² Department of Astronomy, University of Arizona, 933 North Cherry Avenue, Tucson, AZ 85721.

in the ejecta, allowing a very precise probe of the nucleosynthesis in the SN explosion. Because of their low mass, thermonuclear SNe (SNe Ia) have very strong gamma-ray signals and gamma rays make ideal probes of the SN Ia mechanism.

As the shape of the light-curve peak (important in calibrating SNe Ia for use as cosmological probes) is a direct function of the ^{56}Ni decay chain, determining the distribution of ^{56}Ni in SNe Ia is a primary goal of SN Ia studies. At the elemental level, the same diagnostics used in gamma-ray line studies are also present in the optical and infrared emission, and most current studies concentrate on that wavelength range. However, optical and infrared studies require a much more in-depth knowledge of the ejecta characteristics and suffer as a result of uncertainties in this knowledge. Gamma-ray emission studies have a number of features that allow a direct interpretation of the observations and a more exact estimation of the ^{56}Ni yield. The prompt emission lines from gamma rays rely on the production of one isotope (^{56}Ni), and the determined abundances do not suffer from line blends of a number of comparable isotopes as they do in the optical or infrared. In addition, the dominant opacity for gamma rays in the energy range of most gamma-ray lines is Compton scattering that varies smoothly with wavelength and depends only weakly on the composition. The gamma-ray emission lines are produced by the decay of ^{56}Ni and its decay product ^{56}Co , which are insensitive to the ionization state of these isotopes. In contrast, the opacities in the optical and infrared are dominated by a complicated combination of the line opacities from all the elements in the ejecta. Beyond the difficulty of merely including this forest of lines, the line opacities will depend sensitively on both the composition and ionization state of the ejecta. Gamma-ray emission is a much more straightforward, and ultimately more accurate, probe of the ^{56}Ni yield in SNe.

Despite the promise of studying prompt emission, only three SNe Ia have even been observed with gamma-ray telescopes, resulting in only a single, weak detection (SN 1991T) and two upper limits (SN 1986G and SN 1998bu).³ In fact, although the probability to detect prompt emission is predicted to be far higher for thermonuclear SNe than for core-collapse SNe, the two strongest detections have been from an SN of the latter type. SN 1987A was detected at 847 and 1238 keV (from ^{56}Co decays) by the *Solar Maximum Mission (SMM)* instrument (Matz & Share 1990) and with balloon-borne instruments (Mahoney et al. 1988; Rester et al. 1989; Teegarden et al. 1989; Tueller et al. 1990; Kazaryan et al. 1990; Ait-Ouamer et al. 1990) and at 122 keV (from ^{57}Co decays) by the *Compton Gamma Ray Observatory (CGRO)* OSSE instrument (Kurfess et al. 1992).

Even so, the number of gamma-ray transport codes used in the literature to study SNe Ia exemplifies the importance of these diagnostics. Preliminary comparisons between these simulations reveal that the predicted fluxes vary considerably. Indeed, the variation caused by different codes was larger than the variation caused by different explosion models with the same code. Disentangling the differences between codes has been complicated by the fact that the work in the literature does not use the same set of SN explosion models. In addition, most of the published work is limited to line fluxes, and different authors use different definitions of the line flux (i.e., whether the line flux results from the escape fraction of the photons in the specified line or from the convolution of an assumed

instrument response over a simulated spectrum). In this paper we eliminate the earlier confusion by directly comparing seven of the major codes used for gamma-ray line transport, using the same initial progenitors:

1. Müller et al. (1991) and Höflich et al. (1992) simulated emission from delayed detonation models in anticipation of *CGRO* observations of SN 1991T. That ongoing effort, utilizing the MC-GAMMA code, produced a number of papers, many of which studied the energy deposition in SN ejecta. A comprehensive paper by Höflich et al. (1998a, hereafter HWK98) explored various aspects of gamma-ray line emission, including displaying spectra, line fluxes, line ratios, and line profiles for nine SN Ia models. More recently, they have also explored potential ramifications of asymmetry on the line fluxes and line profiles of SN Ia emission (Höflich 2002). We include this code in our study, referring to it as “Höflich.”

2. Shigeyama et al. (1993) simulated gamma-ray emission for two SN Ia models, including the 1991T model, W7DT. Kumagai followed up that work by simulating more models (including HECD) and treating the hard X-ray/gamma-ray emission from their models (Kumagai & Nomoto 1997; Kumagai et al. 1999), and more recently by studying the SN contribution to the cosmic gamma-ray background (Iwabuchi & Kumagai 2001). We include this code in our study, referring to it as “Kumagai.”

3. Other simulation efforts have been motivated by predicted performances of specific missions and/or studies of energy deposition in SN ejecta. Burrows & The (1990) studied X-ray/gamma-ray emission from SNe Ia in anticipation of the launch of the COMPTEL and OSSE instruments on *CGRO*, following earlier, similar studies of SN 1987A (Bussard et al. 1989; The et al. 1990). That work investigated the energy deposition in SNe (The et al. 1994), as well as the SN contribution to the cosmic gamma-ray background (The et al. 1993). Milne et al. (2000, 2002) used simulated gamma-ray line fluxes of SN Ia models from this code to predict the performance of an Advanced Compton Telescope. We include this code in our study, referring to it as “The.”

4. Isern et al. (1996, 1997) and Gómez-Gomar et al. (1998) all displayed results of an ongoing study of gamma-ray emission from a range of SN Ia models. Those studies have concentrated on the potential for the *INTEGRAL* satellite to detect that emission. We include this code in our study, referring to it as “Isern.”

5. Pinto et al. (2001) employed the FASTGAM code to study the X-ray/gamma-ray emission from Chandrasekhar versus sub-Chandrasekhar mass models of SNe Ia. This code was first developed to study emission from SN 1987A (Pinto & Woosley 1988).

6. The three-dimensional Maverick code (Hungerford et al. 2003) was developed to study asymmetries in core-collapse SNe. The physical processes included in Maverick were chosen to match those in FASTGAM, although the implementation techniques of these processes differed at the detailed level. We include the FASTGAM and Maverick codes in our study, referring to them as “Pinto” and “Hungerford,” respectively.

7. In support of an effort to develop two next-generation gamma-ray telescopes, an Advanced Compton Telescope (Boggs & Jean 2001) and a High-Resolution Spectroscopic Imager (Harrison et al. 2003), Boggs (2004) simulated line profiles for SN Ia models. We include this code in our study, referring to it as “Boggs.”

In § 2 we introduce the simulation techniques employed by the seven groups and compare the physics that went into them.

³ For this work, we distinguish “prompt” emission (^{56}Ni and ^{56}Co decays) from “SNR” and/or diffuse emission (such as ^{44}Ti , ^{26}Al , and ^{60}Fe decays).

In § 3 we compare the spectral results from all codes and describe what alterations were made to the codes to achieve agreement between all groups. In § 4 we run a single code (The) with various models and compare the different results possible for different explosion scenarios. In § 5 we compare these simulated spectra with the *SMM* observations of SN 1986G and the *COMPTEL* and *OSSE* observations of SN 1991T and SN 1998bu.

2. DECAY AND TRANSPORT PHYSICS

In order to understand the differences between the simulation techniques used by the various groups in this comparison, we must first lay out the basic physical picture of the problem we are representing numerically. For the purposes of determining the high-energy spectrum (roughly from 30 keV to 4 MeV) at the epochs of interest (10–150 days), the assumption of a homologously expanding SN ejecta is valid. The ejecta composition includes radioactive species such as ^{56}Ni and ^{56}Co , the decay of which provides the gamma-ray line photons that generate the line and, through scatter interactions, continuous gamma-ray spectrum. The basic interaction processes involving these photons are pair production (PP), photoelectric (PE) absorption, and Compton scattering off free and bound electrons. Figure 1 shows a plot of cross sections for these interactions as a function of energy, which shows that the absorptive opacities, PE and PP, are only dominant at low (<150 keV) and high (>10 MeV) energies, respectively. The majority of the energy range discussed is dominated by Compton scattering interactions.

As discussed in detail by Ambwani & Sutherland (1988), the picture described above is well suited for Monte Carlo transport methods. Since six of the seven groups in our collaboration have employed this technique (Höflich, Hungerford, Isern, Kumagai, Pinto, and The), we briefly recap the major points described by Ambwani & Sutherland (1988). The fundamental advantage of Monte Carlo is its ability to accommodate very complicated physical processes in the transport. This is accomplished by simulating the *microphysics* of the photon's propagation through the SN ejecta. The principle is very straightforward: the mass of nickel atoms in the input model implies a certain amount of radioactive decay luminosity. Monte Carlo packets (which represent some quantum of photon luminosity) are then launched in proportion to the decay rate and the mass distribution of nickel atoms. Each packet's energy is chosen in proportion to the branching ratios of the possible decay lines and its initial direction is picked at random, assuming isotropic emission. The emitted packet is then allowed to propagate through the ejecta, interacting with the material through scattering and absorption. This is a microscopic treatment of the transport in the sense that each individual packet of photons is tracked through each individual interaction.

The likelihood of a photon experiencing an interaction during its flight is dictated by the total cross section for interaction (σ_{tot}). When an interaction occurs, the type of interaction, scatter or absorption, is chosen randomly in proportion to the ratio of $\sigma_{\text{scat}}/\sigma_{\text{tot}}$ or $\sigma_{\text{abs}}/\sigma_{\text{tot}}$. The well-described microphysics of the PP and PE absorption and the Compton scatter process are explicitly taken into account for each packet interaction and are thus treated with no approximation. When a packet's path brings it to the surface of the ejecta, it is tallied into the escaping SN spectrum. Likewise, if the path ends in an absorption, the packet's energy is deposited into the ejecta. In this way, the Monte Carlo transport technique allows for

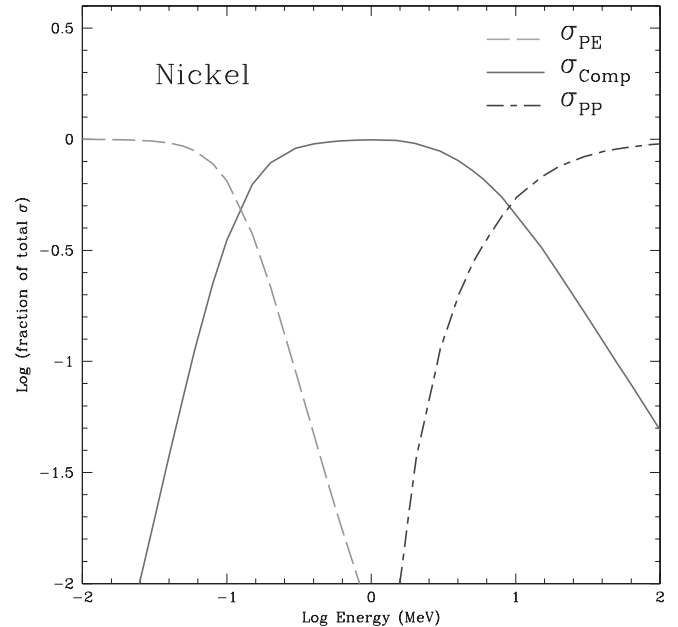


FIG. 1.—Cross sections for photon interactions in nickel. Compton scattering (*solid line*) dominates over photoelectric absorption (*dashed line*) and pair production (*dot-dashed line*) over the energy range 0.1–10 MeV. [See the electronic edition of the *Journal* for a color version of this figure.]

straightforward calculation of the emergent hard X-ray and gamma-ray spectrum, as well as energy deposition into the ejecta via photon interactions.

If the emerging line profile of the gamma-ray decay lines is the only quantity of interest, semianalytic techniques alone, as employed by Boggs in this comparison, can be effectively used as well. The Compton equation describes the energy shift a photon experiences upon suffering a Compton scatter. For the decay lines we are interested in ($E \sim 1$ MeV), a single Compton scatter generally shifts the photon's energy out of the decay line profile. This means that the line profiles in the emergent spectrum arise primarily from photons that escape the ejecta without any interaction, with a secondary contribution from forward-scattered Compton photons. The line profiles can thus be calculated analytically by multiplying the emitted luminosity, as determined from the mass distribution of radioactive species in the ejecta, by the factor $e^{-\tau}$, where τ is the total optical depth from the emission point to the surface of the ejecta. Analytical techniques such as this provide an invaluable test of the more computationally intensive Monte Carlo technique described above.

Regardless of technique chosen, bringing the physical picture to a numerical representation requires a series of computational decisions. In the following subsections we review the physics pertinent to these computational choices. These choices fall into three primary categories:

1. Description of the ejecta (differential velocity, density evolution).
2. Photon source parameters (lifetimes and branching ratios, positron annihilation, ejecta effects, weighting).
3. Opacities for photon interactions (Compton scattering, photoelectric absorption, pair production, and bremsstrahlung emission).

Table 1 lists the various codes and provides information regarding the numerical implementations of the physics discussed below.

TABLE 1
CHARACTERISTICS OF SEVEN GAMMA-RAY TRANSPORT ALGORITHMS

Simulation Creator or Name	References	Monte Carlo	Tag or Spectrum ^a	Bin Width at 847 keV (keV)	Line Broadening ^b (§ 2.1.1)	Density Evolve ^c (§ 2.1.2)	Positronium Fraction $f(\text{Ps})$ (§ 2.2.2)	Time Dilation ^d (§ 2.2.3)	Source Evolve ^e (§ 2.2.3)	Interactions Treated ^f (§ 2.3)
Boggs	1	N	T	2.8	Y	Y	...	Y	Y	CS, PE
Pinto	2	Y	S	2.4	Y	Y	0.0	N	N	CS, PE, PP
Höflich.....	3	Y	S	2.4	Y	N	1.0	Y	N	CS, PE, PP
Isern.....	4	Y	S	2.1	Y	Y	1.0	Y	N	CS, PE, PP
Kumagai.....	5	Y	T	50	N	N	0.0	N	N	CS, PE, PP
Hungerford.....	6	Y	T	0.5	Y	N	0.0	N	N	CS, PE, PP
The	7	Y	T	40	N	N	1.0	N	N	CS, PE, PP

^a Is the line flux derived from determining the escape fraction of “tagged” line photons or extracted from the spectrum and subject to line blending and continuum contamination?

^b Are the photons emitted with Doppler broadening as a result of the differential expansion of the ejecta?

^c Does the algorithm evolve the ejecta density after the photon emission to account for nonzero crossing times?

^d Are the relativistic effects of time dilation on the decay rate included?

^e Does the algorithm account for the effect of requiring simultaneous photon arrival from the near/far side of the ejecta?

^f The interactions treated are CS = Compton scattering, PE = photoelectric absorption, PP = pair production.

REFERENCES.—(1) Boggs 2004; (2) Pinto et al. 2001; (3) Höflich et al. 1998; (4) Isern et al. 1997; (5) Kumagai & Nomoto 1997; (6) Hungerford et al. 2003; (7) Burrows & The 1990.

2.1. Ejecta

For the different explosion models, the ejecta is determined by mapping the model into spherical Lagrangian mass zones and expanding this ejecta homologously outward with time. Taking snapshots in time of this ejecta, each gamma-ray calculation uses the density, radius, velocity, and composition of the ejecta for these mass zones.⁴ Some codes simply take the position of the ^{56}Ni and ^{56}Co , but others include the motion of the ejecta at varying levels of sophistication. The two major velocity effects are the differential motion and the density reduction due to expansion.

2.1.1. Differential Velocity

Since the radioisotope is distributed in velocity space and the opacity depends on the relative velocities, the ejecta velocity will affect the propagation of the photon packets. The packets are created with a decay line energy in the comoving frame of the surrounding ejecta but are tallied in the rest frame of the observer. The Doppler shift between these two frames is the dominant source of broadening in the line profiles. In Figure 2 we show the amount of line broadening possible for four SN Ia models. In addition, as the packet propagates through the ejecta, its energy, as measured in the local comoving ejecta frame, is constantly changing. Since interaction cross sections are energy dependent, the opacity through the ejecta for the packet will be different from the case in which ejecta velocity is neglected. For our scenario, this is a small effect, as our dominant opacity (Compton scattering) is a slowly varying function of energy.

The Boggs, Höflich, Hungerford, Isern, and Pinto algorithms included the ejecta velocity effects, allowing them to calculate detailed line profiles (Table 1).

2.1.2. Density Evolution

Assuming that the decision was made to account for ejecta velocity effects, one must then choose whether to allow this motion to feed back on the densities throughout the ejecta. The photon packet does not traverse its path infinitely quickly. Indeed, there is some flight time associated with each packet trajectory, and during this flight time, the ejecta undergoes expansion. This results in lower densities, and thus lower opacities, as the packet propagates through the star. The alternative to treating this expansion is to assume that the transport takes place within a differential time slice dt , over which the hydrodynamic quantities do not evolve at all. For a homologously expanding ejecta, the density falls off simply as t^{-3} , making this feedback effect easy to implement. However, accounting for it is only a partial step toward a time-dependent treatment of the problem. The source of the photon packets must also be treated in a time-dependent fashion in order to be self-consistent. Unfortunately, the implementation of the source's time dependence is not trivial in a Monte Carlo treatment.

Pinto allowed for the ejecta expansion to feedback on the densities. The semianalytic technique employed by Boggs accounted for both the expansion feedback and the time dependence of the photon source (i.e., photons from the far side of the ejecta take longer to arrive at the detector and must be launched at an earlier time during the explosion; see § 2.2.3).

⁴ The three-dimensional codes must first map the ejecta into a three-dimensional grid. The number and type of nuclei treated in each code vary slightly, and abundances were interpolated to match each code separately.

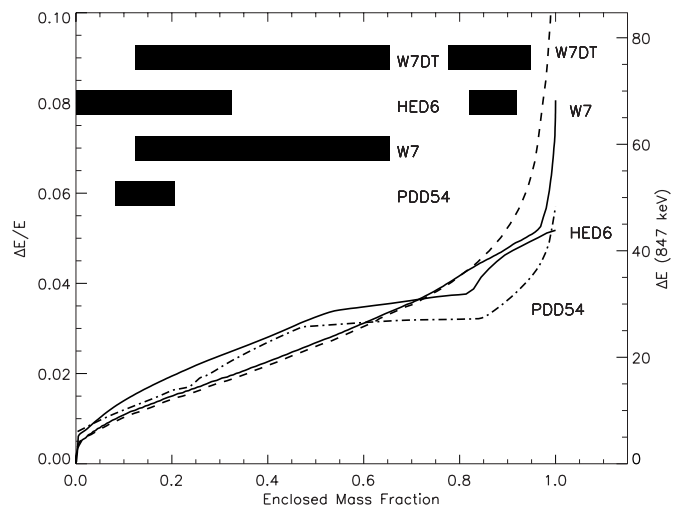


FIG. 2.—Line shifting due to the expansion of the ejecta of four SN models. The fractional line shift due to the expansion of the ejecta is plotted on the left axis, while the shift for the 847 keV line is shown on the right. For reference, ^{56}Ni -rich regions of the ejecta are shown in the upper left as thick, horizontal bars.

2.2. Photon Source

Differences in the gamma-ray sources include not only ^{56}Ni and ^{56}Co decay times and branching ratios but also the emission from positron annihilation. The actual photon emission also depends on the ejecta. Finally, the method of weighting the packets can also pose a problem when normalizing the escaped packet counts into physical flux units.

2.2.1. Decay Times and Branching Ratios

The source of photons for these high-energy calculations is exclusively gamma-ray line emission from the decay of various radio isotopes present in the SN ejecta. The fundamental decay chain is that of the radio isotope ^{56}Ni . The SN explosion synthesizes ^{56}Ni , which promptly decays via electron capture to ^{56}Co with a mean lifetime of ~ 8.8 days. The ^{56}Co produced in this decay is also unstable, although with a longer lifetime (~ 111.4 days). However, we expect the errors caused by the decay times to be less than $\sim 5\%$ (Fig. 3).

We show in Table 2 half-lives from the Nuclear Data Sheets (Junde 1999) and branching ratios from the 8th edition of the Table of Isotopes (Firestone 1996). It is apparent from Table 3 that earlier versions of these tables (and other tables, such as the “Table of Radioactive Isotopes”; Browne & Firestone 1986) contained lifetimes that were as long as 113.7 days mean lifetime for ^{56}Co and as short as 8.5 days mean lifetime for ^{56}Ni . This has led to confusion in the literature as to the correct values.

Whereas the ^{56}Ni decay always proceeds via electron capture, the ^{56}Co decay proceeds through either electron capture (about 81% of decays) or positron production (roughly 19% of decays).⁵ Shown in Table 2 are the relative abundances of the

⁵ It has been suggested (Mochizuki et al. 1999) that the ionization state of the gas can affect the electron capture decay rates in SN remnants, since these decays (^{56}Ni , ^{56}Co , ^{44}Ti) proceed mainly by capturing inner-shell electrons. This effect cannot be important in the preremnant phase, those times before shocks with the circumstellar material have heated the gas to millions of degrees. The gas temperature in the SN at times considered in this work is always far too low for inner shells to have a significant vacancy probability. Further, the timescale over which atoms with an inner-shell vacancy due to nonthermal ionization fill that shell by relaxation from outer shells is far smaller than the mean time between ionizations. The decay rates are thus essentially the zero-ionization (laboratory) values, and these are the values we have employed.

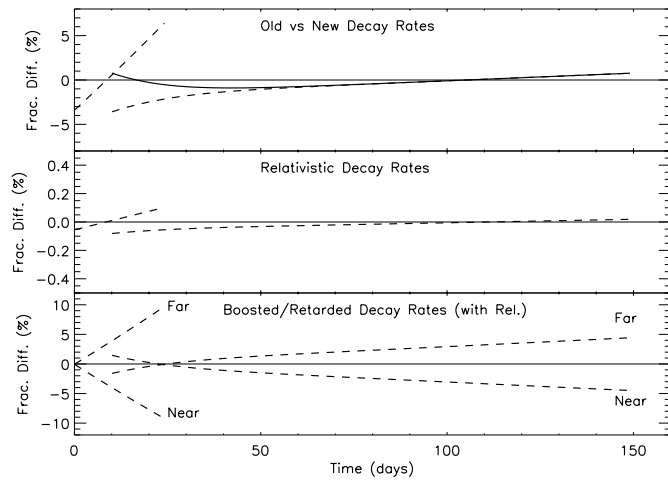


FIG. 3.—Nickel and cobalt decay rates. The top panel shows the fraction change in the decay rates for ^{56}Ni and ^{56}Co assuming mean lifetimes of 8.8 and 113.7 days rather than 8.5 and 111.5 days (*dashed lines*). The simplified ^{56}Co decay rate used in HWK98 compared with the lifetimes of 8.5 and 111.5 days is also shown (*triple-dot-dashed line*). The middle panel shows the fractional change in the decay rates produced by considering the relativistic effects of the ejecta's expansion velocity on the decay rates. The bottom panel shows the effect of the boosting/retarding of the decay rate to synchronize all photons to arrive simultaneously with photons from the center of the SN ejecta. The ejecta velocity is assumed to be $10,000 \text{ km s}^{-1}$ in the lower two panels, a relatively large value for ^{56}Ni -rich ejecta. Bear in mind that until the ejecta becomes thin to gamma rays, the emission from the decays near the surface on the near edge will dominate the integrated emission.

dominant lines from the ^{56}Ni and ^{56}Co decays. Note that these values refer to the number of photons emitted per 100 decays of the respective isotope (i.e., this includes the effects of the 19% positron production branching ratio). Clearly, the dominant branches, both for studies of gamma-ray line emission and for studies of the energy deposition, are the 158, 812, 847, and 1238 keV lines. The exact values for branching ratios and lifetimes of these radioactive decays are subject to updates and revisions, as one might expect. As a result, the suite of values used in a gamma-ray transport code are chosen from a range of possibilities available in the refereed literature.

For the most part, the values adopted from different references have no noticeable affect on the calculated spectra. The only significant variations in adopted branching ratios from earlier works to the current simulations were with the Höflich code. In previous works, the Höflich code adopted 0.74 for the 812 keV line of ^{56}Ni decay rather than the 0.86 employed by the other groups. Furthermore, in previous simulations with the

TABLE 2
IMPORTANT GAMMA-RAY LINE FOR ^{56}Ni AND ^{56}Co DECAYS

^{56}Ni DECAY		^{56}Co DECAY	
Energy (keV)	Intensity (photons/100 decays)	Energy (keV)	Intensity (photons/100 decays)
158.....	98.8	847	100
270.....	36.5	1038	14
480.....	36.5	1238	67
750.....	49.5	1772	15.5
812.....	86.0	2599	16.7
1562.....	14.0	3240 ^a	12.5

NOTES.—Lines studied in this work are listed in bold font. All ratios are from the 8th Table of Isotopes.

^a This line is the sum of a three-line complex.

TABLE 3
HISTORICAL SOURCES OF DECAY HALF-LIVES

Source of Half-Lives	References	$\tau(^{56}\text{Ni})$ (days)	$\tau(^{56}\text{Co})$ (days)
Nuclear Data Sheets.....	1	6.075	77.233
Table of Isotopes (8th).....	2	5.9	77.27
Table of Radioactive Isotopes	3	6.10	77.7
Table of Isotopes (7th).....	4	6.10	78.8
Table of Isotopes (6th).....	5	6.1	77

REFERENCES.—(1) Junde 1999; (2) Firestone 1996, p. 249; (3) Browne & Firestone 1986, p. 56-2; (4) Lederer & Shirley et al. 1978, p. 160; (5) Lederer et al. 1967, p. 189.

Höflich code, it was assumed that the positron production branch left the ^{56}Fe daughter nucleus always in its ground state (Müller et al. 1991). This led to branching ratios for the gamma-ray lines from excited ^{56}Fe being reduced from the published values by the 19% positron production branching ratio.

2.2.2. Positron Decay

Absent from Table 2 are the 511 keV line and the positronium continuum, which result from the positron production branch of the ^{56}Co decay. These positrons are created with ~ 600 keV of kinetic energy that must be transferred to the ejecta before the positron can annihilate with electrons in the ejecta. It is usually assumed that during the epoch of interest for gamma-ray line studies (≤ 150 days), positrons thermalize quickly and thus have negligible lifetimes, annihilating in situ. Detailed positron transport simulations (Milne et al. 1999) have shown that this is not a wholly correct assumption at 150 days; however, only a small error is introduced by making this assumption. Although it is reasonable to assume that the positrons annihilate promptly, in situ, the nature of the resulting emission is not clear. Depending on the composition and ionization state of the annihilation medium, the positron can annihilate directly with an electron (and produce two 511 keV line photons in the rest frame of the annihilation), or it can form positronium first. If positronium is formed (and the densities are low enough to not disrupt the positronium atom), 25% of the annihilations occur from the singlet state. Singlet annihilation gives rise to two 511 keV line photons, as with direct annihilation. However, 75% of annihilations occur from the triplet state, which gives rise to three photons. As the three photons share the 1022 keV of annihilation energy, a continuum is produced. This continuum increases in intensity up to 511 keV and abruptly falls to zero.

The resulting spectrum can thus be characterized by the positronium fraction, $f(\text{Ps})$, a numerical representation of the fraction of annihilations that form positronium (e.g., Brown & Leventhal 1987):

$$f(\text{Ps}) = \frac{2.0}{1.5 + 2.25(A_{511}/A_{\text{posit}})}, \quad (1)$$

where A_{511} and A_{posit} are the observed 511 keV line and positronium three-photon continuum intensities, respectively. Positronium fractions range between 0 and 1, with most researchers assuming that SN annihilations have a similar positronium fraction as the Galaxy.⁶ Utilizing wide field of view TGRS observations of Galactic annihilation radiation, Harris et al. (1998) estimated the positronium fraction to be 0.94 ± 0.04 .

⁶ Note that the positronium fraction function cannot accept continuum fluxes of exactly zero. If $A_{\text{posit}} = 0.0$, then $f(\text{Ps}) = 0.0$, independent of the equation.

Similarly, utilizing *CGRO* OSSE observations of the inner Galaxy, Kinzer et al. (2001) estimated the positronium fraction to be 0.93 ± 0.04 , both values in agreement with theoretical estimates of interstellar medium (ISM) positron annihilation. However, the composition of SN Ia ejecta is far different than the ISM, being dominated by intermediate and heavy elements rather than hydrogen and helium. Thus, ISM annihilation is completely different than SN ejecta annihilation. Likewise, the Galactic annihilation radiation measured by OSSE is a diffuse emission, and thus it is distinct from the in situ annihilations that occur in SN Ia ejecta within 200 days of the SN explosion. The expectation is that charge exchange with the bound electrons of these intermediate and heavy elements would lead to SN ejecta having a positronium fraction of at least 0.95. However, a zero positronium fraction for annihilations that occur in SN ejecta cannot be ruled out.

For our purposes here, it suffices to say that the expected spectrum from positron annihilation is uncertain, and the individual members of this comparison team have adopted positronium fractions of either 0 (Hungerford, Kumagai, and Pinto) or 1 (Höflich, Isern, and The); see Table 1 for a summary. The three groups employing positronium fractions of 1 adopted the energy distribution of the positronium continuum treatment in Ore & Powell (1949).

2.2.3. Ejecta Effects on Decay

The motion of the ejecta can also change the decay rate. The decay equations for ^{56}Ni and ^{56}Co decays in a stationary medium are

$$\frac{1}{\text{Ni}_0} \left(\frac{d\text{Ni}}{dt} \right) = -\frac{1}{\tau_{\text{Ni}}} \exp\left(\frac{-t}{\tau_{\text{Ni}}}\right), \quad (2)$$

$$\frac{1}{\text{Ni}_0} \left(\frac{d\text{Co}}{dt} \right) = \frac{-1}{\tau_{\text{Co}} - \tau_{\text{Ni}}} \left[\exp\left(\frac{-t}{\tau_{\text{Co}}}\right) - \exp\left(\frac{-t}{\tau_{\text{Ni}}}\right) \right], \quad (3)$$

where τ_{Ni} and τ_{Co} are the mean lifetimes of the isotopes, Ni_0 is the ^{56}Ni produced in the SN explosion, and t is the time since explosion. For a given model time ($t = t_m$), these equations can be solved for the number of nickel and cobalt atoms that will decay during an infinitesimal time slice dt . These equations still hold for a finite time step Δt , assuming that Δt is much less than the lifetime τ . Strictly speaking, the lifetimes (τ_{Ni} and τ_{Co}) in the above equations are in the frame of the isotope, which is moving relative to an external observer. Since the velocity of the ejecta can be upward of 10,000 km s^{-1} , an exact treatment of the decay rate must include a conversion to the frame of the external observer. This relativistic effect is proportional to $\gamma = (1 - v^2/c^2)^{-1/2}$ and is only a 0.1%–0.2% effect overall (Fig. 3). Aside from Boggs, none of the codes include this effect.

More important is the flight time of the photons through the ejecta. In the context of equations (2) and (3) it is straightforward to point out where to accomplish this. Emission from the near side of the ejecta should be calculated from the above equations using a retarded time relative to the far side. In this way, photons from the front and back of the ejecta arrive simultaneously at the detector. Figure 3 shows the effect these two issues (in the extreme) have on the calculated decay rate. The flight time of the photons introduces less than a 10% error. (NB: The triple-dot-dashed line in Fig. 3 represents the variation in decay rate of cobalt resulting from an approximate form of eq. [3] used in one of the comparison codes.) Again, Boggs's code is the only one that incorporates these effects.

2.2.4. Weighting

The last uncertainty is purely numerical in nature and arises from the weighting (and subsequent normalization) of the photon packets. Combining the decay rate with the branching ratios, which provide a measure of the average number of photons per decay, equations (2) and (3) yield a total photon luminosity ($\mathcal{L}_{\text{phot}}$) of the ejecta (in photons s^{-1}). Given the number of photon packets to be tracked in the simulation ($\mathcal{N}_{\text{packet}}$), the weight of each packet is

$$\mathcal{W}_{\text{packet}} = \frac{\mathcal{L}_{\text{phot}}}{\mathcal{N}_{\text{packet}}}.$$

More complicated weighting algorithms are possible and provide advantages when specialized information is desired. For example, detailed studies of the spectral characteristics for weaker decay lines benefit from emitting a large number of packets at the decay energies of interest. In this way, the signal-to-noise ratio of the spectrum at those weak lines is enhanced beyond what the uniform weighting technique could provide. In any case, the normalization applied via this weight factor can be taken into account from within the transport code itself, or as a postprocess step on the photon packet counts, which result from the base Monte Carlo transport routine. The validity of the normalization is easily tested through the analysis of the integrated line flux light curves for the various decay lines. These light curves can be directly compared with the semianalytic technique discussed above for decay lines with energies greater than about 1 MeV (i.e., where the continuum has a negligible contribution to the spectrum). For our study, all the Monte Carlo algorithms were run using constant weight packets to reduce the complexity of the comparison, but as we shall see, it is the weighting and the subsequent normalization of the flux that caused many of the discrepancies in past simulations (see § 3.4).

2.3. Photon Interaction Processes

Once the decay photons have been created, their propagation through the ejecta is dictated by the three interaction processes mentioned at the start of this section: pair production, photoelectric absorption, and Compton scattering. The major features of the spectrum, with the exception of actual line fluxes, can be understood primarily through the PE absorption and Compton scatter interactions.

2.3.1. Compton Scattering

For the majority of the energy range we are interested in, the Compton scatter interaction off bound and free electrons dominates. This interaction depends only on the total electron density in the ejecta and energy of the incident photon. Since almost all SN Ia ejecta have an electron fraction $Y_e \sim 0.5$, this interaction is only weakly dependent on the composition.

Figure 1 shows the energy dependence of the cross section for Compton scattering as employed by the various groups. This cross section is a smoothly varying function of energy and, in general, is represented by

$$\sigma_{\text{Compton}} = \frac{3\sigma_{\text{T}}}{8\epsilon} \left\{ \left[1 - \frac{2(\epsilon + 1)}{\epsilon^2} \right] \ln(2\epsilon + 1) + \frac{1}{2} + \frac{4}{\epsilon} - \frac{1}{2(2\epsilon + 1)^2} \right\}, \quad (4)$$

where σ_T is the Thomson scattering cross section and ϵ is the ratio of the photon energy to the electron rest mass.

While photoelectric absorption and pair production interactions consume the photon, the scattering process produces a lower energy photon traveling in a new direction. The down-conversion of the photon's energy is the dominant process for populating the hard X-ray continuum, and the exact energy distribution of the outgoing photons is described by the Klein-Nishina (KN) differential scatter cross section. The KN formula is given by (Raeside 1976)

$$\frac{d\sigma}{d\epsilon'} = -\frac{3\sigma_T}{8} \left(\frac{1}{\epsilon}\right)^2 \left[\frac{\epsilon}{\epsilon'} + \frac{\epsilon'}{\epsilon} - 1 + \left(1 - \frac{1}{\epsilon'} + \frac{1}{\epsilon}\right)^2 \right], \quad (5)$$

where ϵ is the photon's incoming energy and ϵ' is the photon's outgoing energy. Given ϵ , many techniques exist for sampling an outgoing energy from this relation. Combining this information with the Compton formula, an outgoing photon direction is then determined. Detailed comparisons of the individual sampling techniques used by the various groups have not been done. However, for the six groups that track the scattered photons, the continuum in their simulations is produced entirely through the scatter interaction. Fortunately, the shape of this Comptonized continuum (200–800 keV) is a direct and sensitive test that the physics of photon-electron scattering has been implemented appropriately.

2.3.2. Pair Production and Photoelectric Absorption Opacities

At low energies (less than ~ 200 keV), the smooth, nearly power-law continuum created from Compton scattering suffers a turnover due to photoelectric absorption effects. Just as in the adoption of values for branching ratios and decay lifetimes, the literature offers more than one reference for choosing absorptive opacities. The PE and PP opacities employed by the various groups in our collaboration can be found from three primary references (Viegle, Hubbell, and ENDL), which provide these cross sections in tabular form (by energy and proton number). Techniques for interpolating cross sections from the provided energy table values varied among the different groups. A number of nuclei species (different proton numbers), which were considered as contributors to these absorptive opacities, were also treated differently in the various codes. These types of variations in the numerical implementation ought to manifest themselves as slight changes in the location of the low-energy spectral cutoff.

In addition, both of these absorptive interactions allow for the possibility of high-energy photon daughter products: annihilation photons for the case of pair production and X-ray fluorescence photons for the case of photoelectric absorption. The decision to include these processes and the technique for implementing them varied among groups. The X-ray fluorescence photons are below the low-energy cutoff and, thus, contribute predominantly to the calculated deposition energy. In this paper we concentrate only on the emergent spectrum and thus do not probe the differences caused by the inclusion of the X-ray fluorescence.

2.3.3. Bremsstrahlung Emission

Another important photon emission process from the ejecta is the bremsstrahlung process of the energetic Compton recoil electrons ($E \leq 3$ MeV; recoiling from Compton scattering events with the primary radioactivity gamma rays). This bremsstrahlung process takes place in all SNe that are powered

by radioactive decay. The large abundance of these electrons gives rise to the dominance of bremsstrahlung photons as the hard X-ray source, i.e., below 30 and 60 keV at 20 and 80 days, respectively, in both models W7 and DD4 (Clayton & The 1991; Pinto et al. 2001). The shape of the bremsstrahlung spectrum emerging from the surface is sensitive to the photoelectric opacity and with the flux, $F(E) \propto E^\alpha$, where α is ~ 1.1 and ~ 1.8 at 20 and 80 days, respectively, for model W7 (Fig. 13 of Clayton & The 1991); the spectral luminosity increases slowly between 1 and 60 keV. The sudden change in the hard X-ray slopes between 10 and 100 keV (from the bremsstrahlung spectrum at lower energies to the Compton scattering spectrum at higher energies) can be used as the signature of this process. None of the simulations in this comparison project included this process.

3. COMPARISONS BETWEEN CODES

The seven codes included in this study have all produced published simulations of SN models. All but the Hungerford code have produced published simulations of specifically SNe Ia. Indirect comparisons between published works from the codes being studied in this paper suggest that different codes reach different answers. Notably, HWK98 and Kumagai & Nomoto (1997) both predict larger line fluxes than Pinto et al. (2001), Milne et al. (2000), or Boggs (2004). However, determining the cause of such spectral variations has been difficult since no single input SN Ia model has been simulated by all groups. While it is generally agreed that SNe Ia are caused by the thermonuclear explosion of an accreting white dwarf, there remains considerable controversy as to the exact nature of the progenitor and the physics behind the development of the burning front: deflagration versus detonation, number of ignition sites (e.g., Livio 2001). These differences have produced a set of SN Ia explosion models in terms of a handful of parameters that form the basis for comparisons with SN observations. In this paper we provide the much-needed direct comparisons by running all seven gamma-ray transport codes on the same set of SN Ia explosion model inputs. The set of three models that were selected for comparisons are DD202C (a Chandrasekhar mass delayed detonation; Höflich et al. 1998b), HED6 (a subluminous, sub-Chandrasekhar mass helium detonation; Höflich & Khokhlov 1996), and W7 (a Chandrasekhar mass deflagration; Nomoto et al. 1984). In Table 4 we show the relevant characteristics of the models. Errors were introduced by imperfections in the conversion of each model into the varied formats required by each code. Typically these errors were 2%–3% of the mass or kinetic energy and were found to have a negligible effect on the Compton scattering dominated portion of the spectra.

For these comparisons, we focus on three aspects of the gamma-ray calculations: the overall spectra, the line profiles, and, the most important observed quantity in the near future, the line flux.

3.1. Overall Spectra

Figures 4–6 show a sequence of spectra from simulations of DD202C, W7, and HED6, respectively. These spectral results arise from current versions of the six Monte Carlo codes employed in this comparison and agree to within the statistical noise except in a few cases. In § 3.3 we describe in detail the necessary corrections that were made to arrive at the current versions. The remaining differences in the spectral simulations can be isolated in terms of the physical processes outlined in

TABLE 4
CHARACTERISTICS OF SN Ia EXPLOSION MODELS

Model Name	Mode of Explosion	References	M_* (M_\odot)	M_{Ni} (M_\odot)	E_{kin} (10^{51} ergs s^{-1})
Algorithm Comparison					
DD202C.....	Delayed det.	1	1.40	0.72	1.33
HED6.....	He-det.	2	0.77	0.26	0.74
W7.....	Deflagration	3	1.37	0.58	1.24
Spanning Explosions					
PDD54.....	Pul. del. det.	4	1.40	0.14	0.35
W7DT.....	Late det.	5	1.37	0.76	1.61
HED8.....	He-det.	2	0.96	0.51	1.00
HECD.....	He-det.	6	1.07	0.72	1.35

REFERENCES.—(1) Höflich et al. 1998b; (2) Höflich & Khokhlov 1996; (3) Nomoto et al. 1984; (4) Höflich et al. 1995; (5) Yamaoka et al. 1992; (6) Kumagai & Nomoto 1997.

§ 2. For example, in Figures 4 and 5 at the earliest epoch, it is clear that the Höflich spectra exhibit a different continuum slope across the rough energy range of 200–800 keV. The shape of the continuum in this portion of the spectrum is dictated primarily by the KN differential scattering cross section, although physical effects such as Doppler corrections for the ejecta velocities may also change the overall spectral slope. Closer inspection of the Compton scatter and Doppler boost routines between Höflich and other codes did not reveal an

obvious cause for this difference, which has a maximum magnitude of order 30% but is much smaller across most of the energy range.

As discussed in § 2.2.2, spectral variations due to differences in the assumed positronium fractions should appear in the 400–550 keV energy range (Figs. 4–6). At late times, one would expect the codes that include the positronium continuum to have slightly higher continuum spectra and weaker lines. There is very little difference between the codes that include a positronium continuum component (Höflich, Isern,

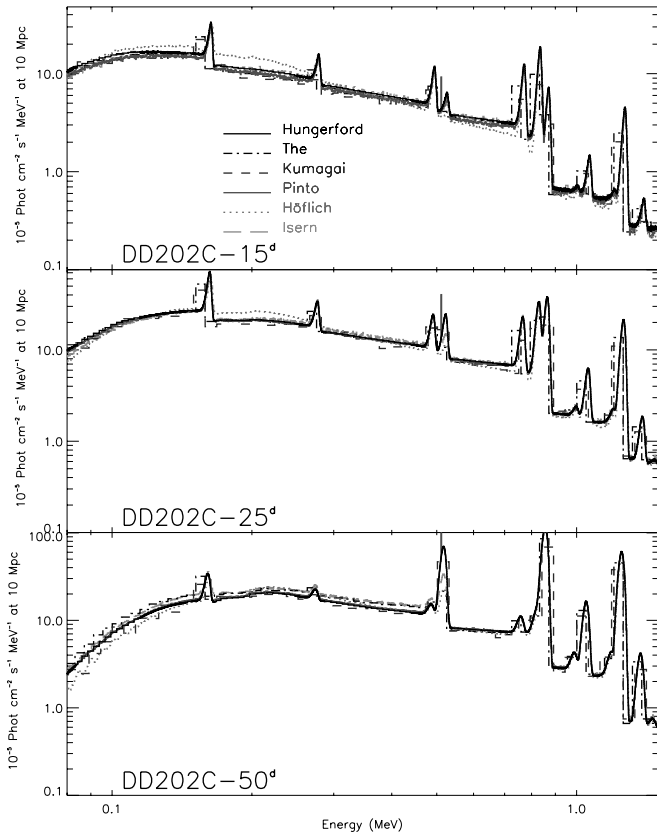


FIG. 4.—Sequence of spectra for the SN Ia model DD202C. The spectra, at 15, 25, and 50 days, show the level of agreement between simulations for both the line and continuum emission. Comparisons between the two algorithms that do not treat line broadening/shifting (The and Kumagai) and the others that do show the early effects of blueshifting. [See the electronic edition of the Journal for a color version of this figure.]

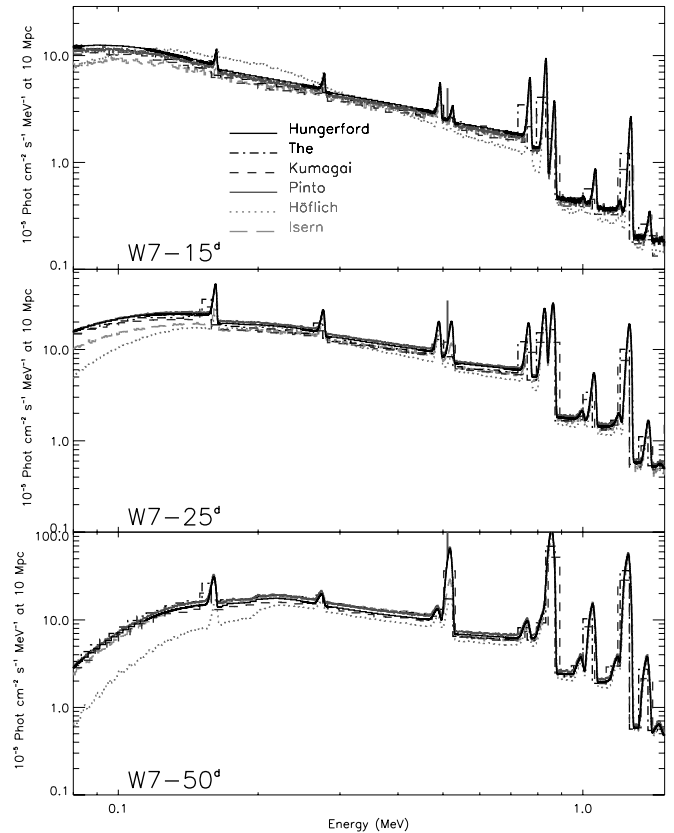


FIG. 5.—Sequence of spectra for the SN Ia model W7. The absence of nickel near the surface of W7 leads to the inhibition of line emission until later times. As with DD202C, the spectra, at 15, 25, and 50 days, show a high level of agreement between simulations for both the line and continuum emission. [See the electronic edition of the Journal for a color version of this figure.]

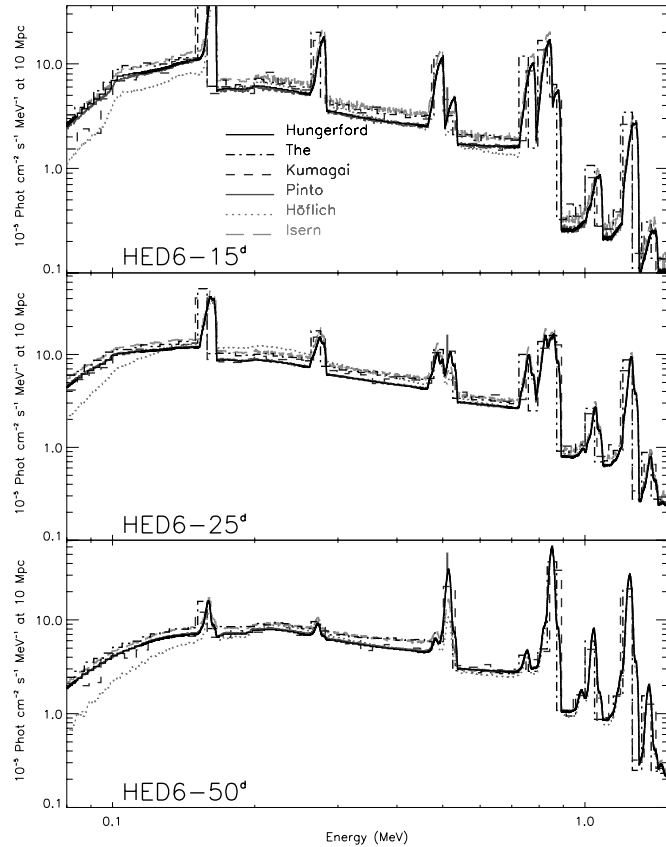


FIG. 6.—Sequence of spectra for the SN Ia model HED6. The spectra, at 15, 25, and 50 days, show a high level of agreement between simulations, in this case for a low-mass model that features early escape of gamma-ray emission. [See the electronic edition of the *Journal* for a color version of this figure.]

and The) and those that do not (Hungerford, Kumagai, and Pinto), but the expected trends seem to hold. As these spectra likely bracket the range of possible annihilation spectral features, the treatment of the positronium fraction primarily affects the strength of the 511 keV line, and it does not dominate the appearance of the continuous spectrum.

There also remain differences in the ≤ 100 keV spectra that exceed statistical fluctuations. These differences likely arise from differences in the implementation of photoelectric absorption opacities. Differing interpolation techniques for the tabular opacities, to account for the difference in number of nuclear species treated, may be responsible for these discrepancies. As the emphasis of this comparison is on the higher energy gamma-ray portion of the spectrum, we did not attempt to resolve these opacity differences.

3.2. Line Profiles

In Figures 7 and 8 we show line profiles of the 1238 keV line and the 812 and 847 keV line complex. The Boggs simulations are specifically of line profiles; thus, they contribute only to these two figures and not the previous three. The Kumagai and The codes did not produce line profiles and are thus not included in these figures. We note that Burrows & The (1990) did simulate line profiles by adopting a technique explained in Bussard et al. (1989), which is similar to the technique explained in Chan & Lingenfelter (1987).

The Boggs line profiles, shown in Figures 7 and 8, do not include the Compton scattered photons from higher energy nuclear lines. The fact that the Boggs line profiles agree very

well with the other line profiles suggests that treating the Compton downscattered photons has only a small effect on the line profiles. These photons would only become important if an instrument's energy resolution is poor enough that it samples beyond the energy ranges shown in these figures.

Although detailed line profile observations require instrument sensitivities beyond those currently available (for all but the nearest SNe), their diagnostic potential for distinguishing between SN Ia explosion models is very strong. Because the line photons arise primarily from noninteracting gamma rays, the line shape is a direct probe of the spatial distribution of ^{56}Ni synthesized in the SN explosion. For a more detailed discussion of the potential for such observations with current and planned missions, see HWK98.

3.3. Line Fluxes

A far easier observation to make, and the quantity more frequently published from theoretical simulations, is the time evolution of integrated line fluxes (gamma-ray light curves). Since the Kumagai and The codes do not include ejecta velocity effects, they compare line emission with the other codes only through integrated flux values, obtained by tallying “tagged” line photons (i.e., a photon created at the gamma-ray line energy is tagged as such and contributes to the integrated flux if it escapes with no interaction).

Such comparisons of the light curves from previously published results in HWK98 (for DD202c and HED6) revealed significant differences in the magnitude and shape of the 812, 847, and 1238 keV light curves from the results presented here. Further inspection of the overall spectra from HWK98 confirmed that the spectra were similar in shape but tended to be brighter by an epoch-dependent factor. Closer study of the Höflich code determined that a postprocess step, required for correct weight normalization of the Monte Carlo packets, was performed incorrectly in the HWK98 spectra (for details see Höflich & Wheeler 2004). When corrected for the appropriate weight factor, which was equal to the total escape fraction for each epoch, the HWK98 spectra roughly agree with the spectral results in this work.

Light-curve results from Kumagai & Nomoto (1997) for model W7 also demonstrated an enhanced flux level, although the light-curve shape was similar to the results found here. Comparisons with previously published W7 spectra (Kumagai & Nomoto 1997; Kumagai et al. 1999; Iwabuchi & Kumagai 2001) reveal consistent results with the overall spectra presented in § 3.1. This points to an offset problem in the generation of the integrated flux data, possibly related to setting the SN at a given distance and/or scalings in the ^{56}Ni mass of the explosion model.

3.3.1. 1238 keV Line Flux

The 1238 keV ^{56}Co decay line is the most straightforward line flux to study. This line is isolated from other lines, and there is little continuum emission to contaminate line flux estimates. We define the 1238 keV line to be all photons with energies between 1150 and 1300 keV. Shown in Figure 9 are the 1238 keV light curves for DD202C, W7, and HED6. For comparison, we include earlier light curves from HWK98 and Kumagai & Nomoto (1997), although those works did not use the same line definitions used in this work.

The HWK98 light curves (DD202c and HED6) are enhanced at early times and slightly fainter than the current simulations at late times, demonstrating the trends from the missing weight normalization (discussed above) and the

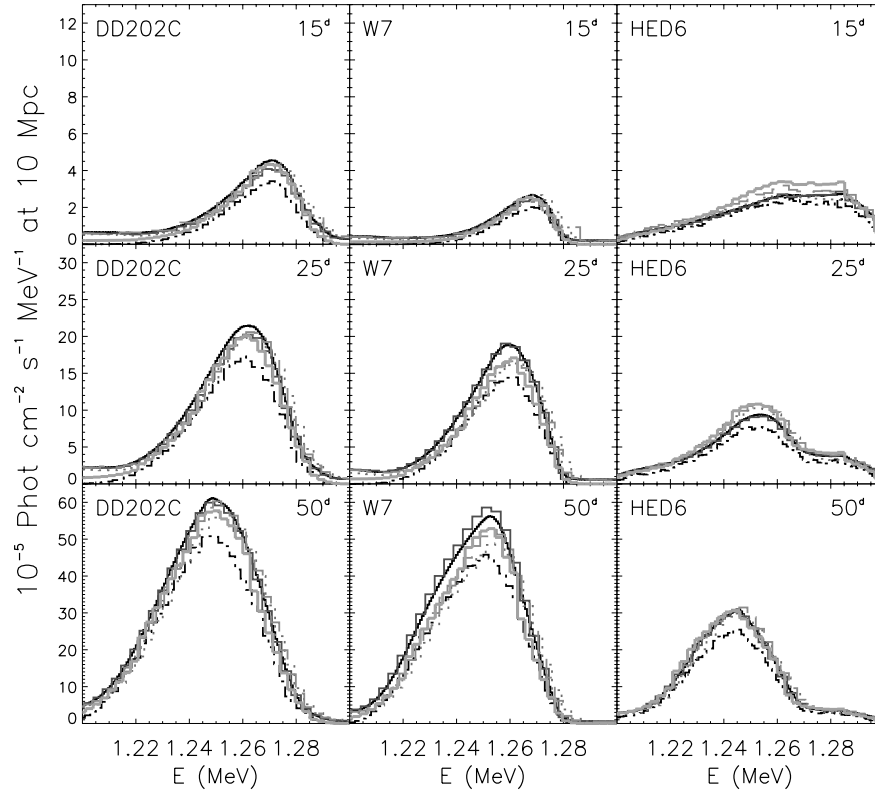


FIG. 7.—Line profiles of the 1238 keV line for the SN Ia models DD202C, W7, and HED6. Although the simulations show noticeable variations, the differences between the Chandrasekhar mass models (DD202C and W7) and the sub-Chandrasekhar mass model (HED6) greatly exceed the variations between simulations. Differentiating between DD202C and W7 is more difficult but is not rendered impossible by the variations between simulations if a sequence of spectra were available for comparison. [See the electronic edition of the Journal for a color version of this figure.]

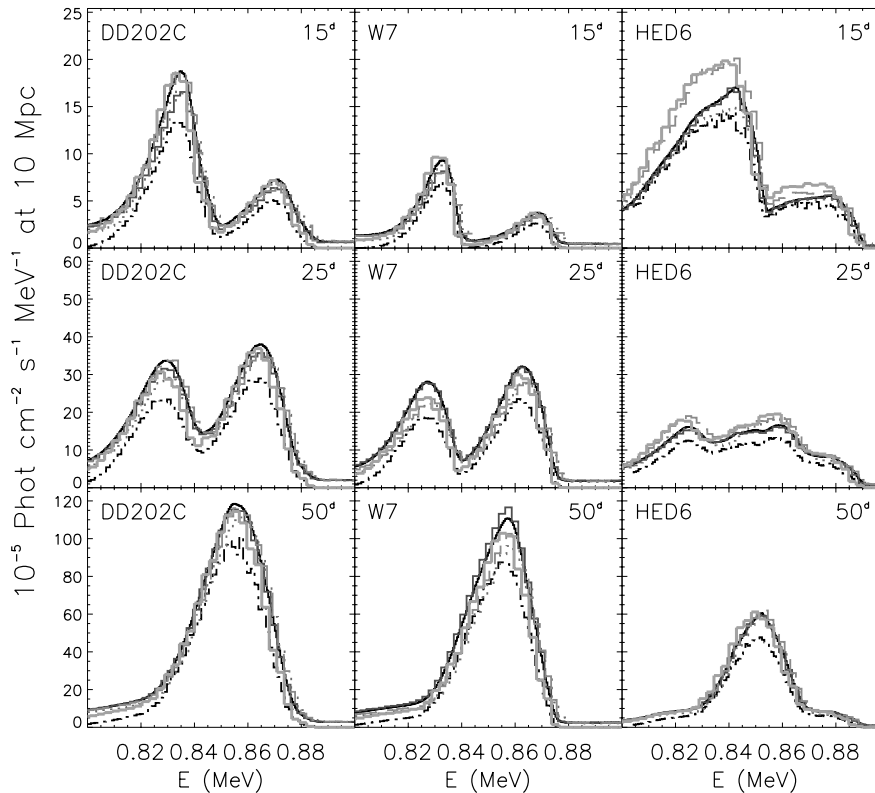


FIG. 8.—Line profiles of the 812 and 847 keV line complex for the SN Ia models DD202C, W7, and HED6. The interpretation is similar to that of the 1238 keV line: the differences between the Chandrasekhar mass models (DD202C and W7) and the sub-Chandrasekhar mass model (HED6) greatly exceed the variations between simulations, and while differentiating between DD202C and W7 is more difficult, it is not rendered impossible by the variations between simulations if a sequence of spectra were available for comparison. [See the electronic edition of the Journal for a color version of this figure.]

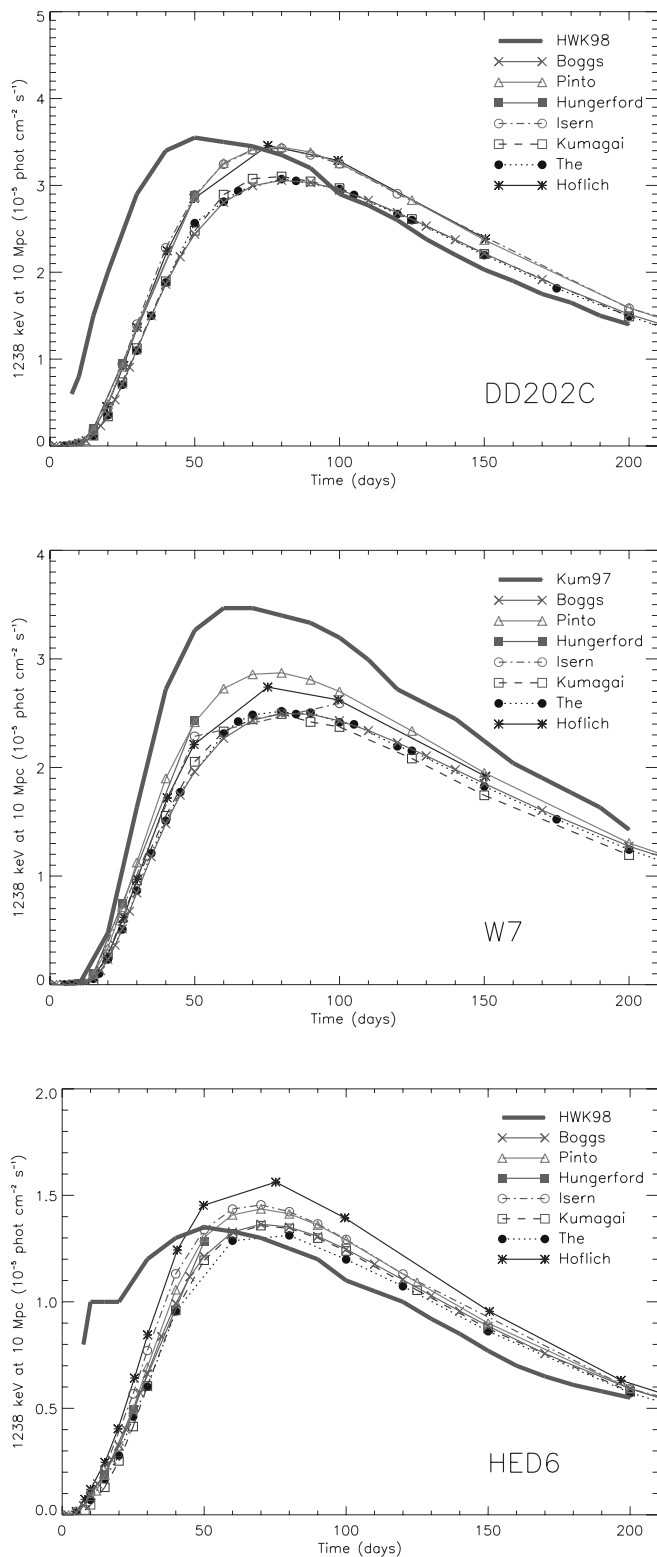


Fig. 9.—Line fluxes of the 1238 keV line for the SN models DD202C (*top*), W7 (*middle*), and HED6 (*bottom*). The line fluxes extracted from the spectra (Höflich, Maverick, FASTGAM, Isern) agree with the line fluxes that result from tagging line photons (The, Boggs, Kumagai). All current simulations predict fainter light curves than shown in previous published results (HWK98 for DD202C and HED6; Kumagai & Nomoto 1997 for W7). Spectral extraction assumed a 1150–1300 keV bandwidth. The HWK98 results are shown with and without the scaling for the escape fraction and branching ratios. Although the line definition in HWK98 differs from that used in this work, the light curves are similar when the corrections are applied. [See the electronic edition of the *Journal* for a color version of this figure.]

lowered ^{56}Co decay branching ratios (see § 2.2.1). The Kumagai & Nomoto (1997) light curve for W7 appears too bright at all epochs, consistent with some offset injected during the calculation of integrated line fluxes.

The three codes that derive line fluxes from tagged photons (The, Kumagai, & Boggs) yielded similar light curves to the other four codes, which obtained line fluxes from spectral extraction techniques. This suggests that the extraction of the line flux from the spectra can be performed in a manner that does not introduce appreciable systematic errors in the light curves. It is worth reiterating that ultimately spectra must be compared with observations in order to infer the nickel production from an actual SN, so the fact that the line fluxes were adequately extracted from the spectra is encouraging for the astrophysical use of these simulations.

3.3.2. 812 and 847 keV Line Fluxes

The two brightest gamma-ray lines occur at 812 and 847 keV. The former is produced by $^{56}\text{Ni} \rightarrow ^{56}\text{Co}$ decays, while the latter is produced by $^{56}\text{Co} \rightarrow ^{56}\text{Fe}$ decays. The high-velocity expansion of the ejecta creates Doppler broadening that blends the two lines. Ultimately, when observed with an instrument that can resolve the spectra, these line profiles will provide a wonderful diagnostic of the nickel distribution. However, the line blending makes quantitative line flux comparisons between codes more difficult. Rather than try to isolate the individual contributions from each line based on the line profile, we have chosen to combine the two lines. Explicitly, we have defined the total flux to be all photons with energies between 810 and 885 keV (ignoring the fact that we include contamination from continuum emission). We assume equal escape fractions (a reasonable assumption for two lines very near in energy) and assign the individual line fluxes by the relative decay rates for each line (which are known at each epoch). For example, at 20 days the decay rate of $^{56}\text{Ni} \rightarrow ^{56}\text{Co}$ decays is 1.83 times the decay rate of $^{56}\text{Co} \rightarrow ^{56}\text{Fe}$ decays. Thus, we assign 65% of the total flux to the 812 keV line and 35% to the 847 keV line.

In Figures 10 and 11 we show the 847 and 812 keV line fluxes for the three models as simulated by all seven codes. Again for comparison, we include earlier light curves from HWK98 and Kumagai & Nomoto (1997). The deviation at late times (>25 days) for the HWK98 812 keV light curve is consistent with the lower adopted branching ratio used in that code (see § 2.2.1). As with the 1238 keV light curves, we find the same good agreement between the current code results.

3.4. Summary of Comparisons

In light of the previous differences in simulated SN Ia gamma-ray spectra, the agreement demonstrated in this comparison is strongly encouraging. The differences between the individual simulations are generally at the 10%–20% level, much less than the differences that result from a range of input explosion models. This is particularly apparent in the nine panels of Figures 7 and 8. There would be no ambiguity as to which is the correct scenario if these three models were compared with actual observations of sufficient sensitivity. While it is true that very similar models might be unresolvable as a result of the current variations between simulations, the level of accuracy required to perform this type of observation will not be realized in the foreseeable future.

Since we have chosen a set of explosion models that probably represent the full range of SN Ia explosions, these models provide an ideal testing ground for gamma-ray transport codes,

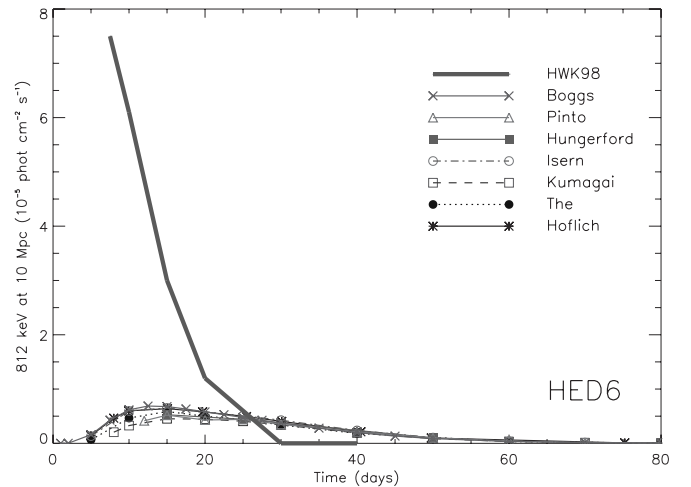
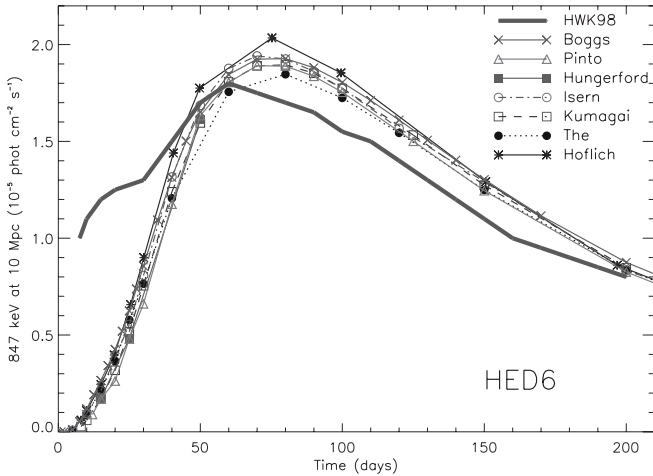
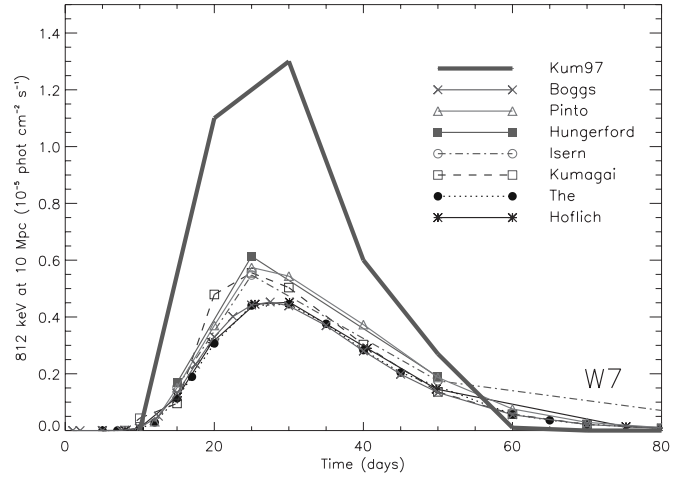
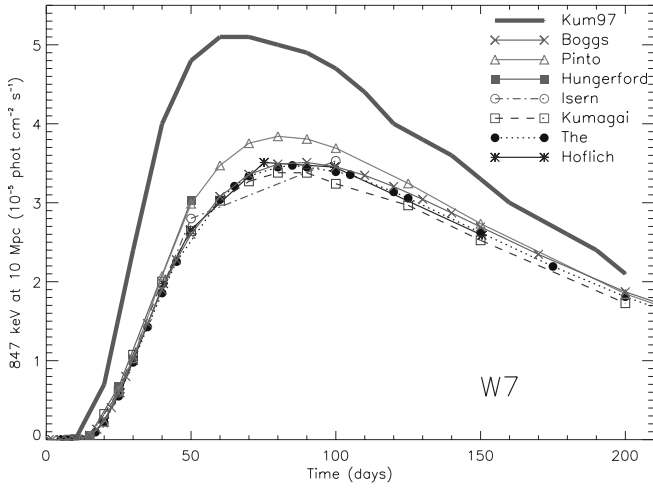
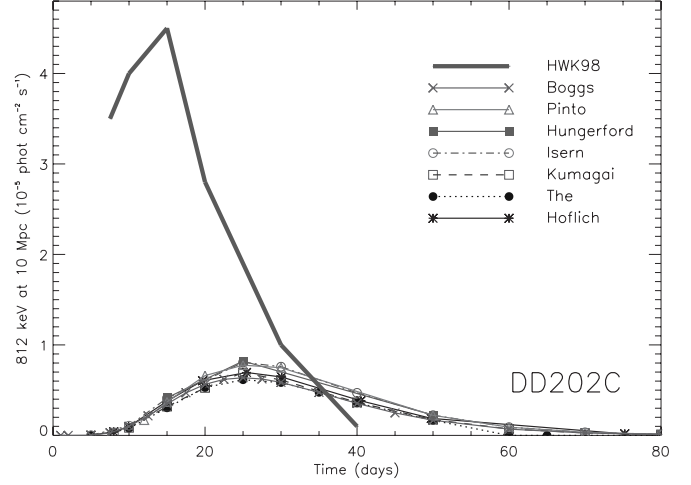
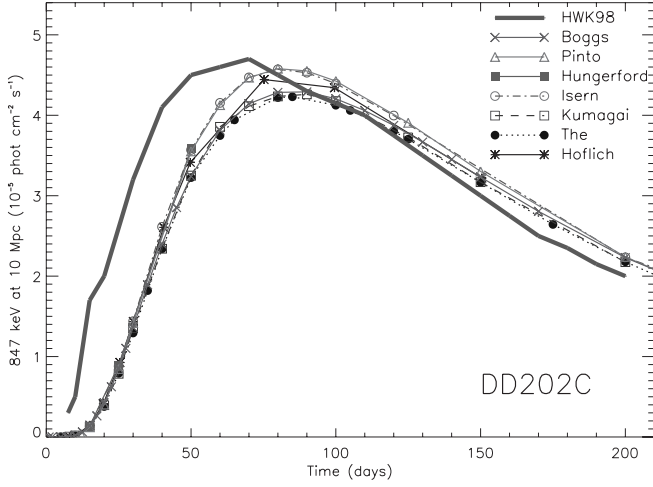


FIG. 10.—Line fluxes of the 847 keV line for the SN models DD202C (*top*), W7 (*middle*), and HED6 (*bottom*). Spectral extraction was more complicated for the 847 keV line than for the 1238 keV line (requiring the assumptions that the 847 and 812 keV escape fractions are equal and that all emission in the 790–900 keV energy band is line emission), but the light curves agree well with the light curves that result from tagging photons. Again, all current simulations suggest less line emission than suggested in HWK98 and Kumagai & Nomoto (1997). In addition, the scaling for escape fraction and branching ratios brings the HWK98 light curves into rough agreement with the other light curves. [See the electronic edition of the *Journal* for a color version of this figure.]

FIG. 11.—Line fluxes of the 812 keV line for the SN models DD202C (*top*), W7 (*middle*), and HED6 (*bottom*). As with the 812 keV line emission, the spectral extraction and tagging light curves agree and are fainter than the HWK98 and Kumagai & Nomoto (1997) light curves. With the scaling for escape fraction and branching ratios, the HWK98 light curves agree fairly well with the other light curves. The HWK98 light curves after 20–30 days fall to zero, faster than the other light curves; this is due to the different definition for the 812 keV line employed in that work. [See the electronic edition of the *Journal* for a color version of this figure.]

and it is likely that codes that get good agreement against the spectra and light curves presented here can be trusted using different explosion models as well.

Having demonstrated that the simulations have converged upon similar solutions for these three models, we explore the range of SN Ia events considered possible (§ 4) and compare these simulations with observations (§ 5).

4. SN Ia LINE FLUXES

With the current agreement of all seven codes for a range of explosion models, we can now use the simulated gamma-ray signal to predict observational differences between the explosion models. Over the next few years, the challenge in gamma-ray observations will be to make a detection of a single, time-averaged flux (requiring a lengthy exposure). The dominant, 847 keV line flux peaks 50 or more days after the SN explosion, so there is ample time for the SN to be detected and identified through optical observations before gamma-ray observations must commence. The 812 keV line evolves on a shorter timescale (10–35 days) and has a fainter peak (limiting its detection to very local SNe). As the SN takes roughly the same timescale to reach the optical peak, gamma-ray observations need to commence a few days before optical peak to contain the 812 keV peak. A large fraction of nearby SNe Ia are detected at peak or later, so this requirement places strict demands on “Target-of-Opportunity” telescopes.

In this section we show line flux light curves for a collection of SN Ia models simulated with the The code. We separate the models into three subclasses based on observational categories: normally luminous, subluminous, and superluminous.⁷

4.1. Normally Luminous SNe Ia

This is the most frequent SN Ia subclass and the best studied. SN 1998bu was considered normally luminous and is grouped in this category (§ 5.3). We compare three models that fit within this subclass, W7 (a Chandrasekhar mass deflagration), DD202C (a Chandrasekhar mass delayed detonation), and HED8 (a sub-Chandrasekhar mass helium detonation). The light curves are shown in the top panel of Figure 12. HED8 creates the least amount of nickel but has nickel near the surface. This leads to HED8 being the brightest model of the three at early epochs, but the faintest model after 150 days. For a sufficiently early observation of a nearby SN, DD202C and W7 are easily distinguished from HED8 based on the 812 keV line (or equivalently, the timing of the rise of the 847 keV line).

4.2. Superluminous SNe Ia

This SN Ia subclass differs from the normally luminous SNe Ia in that the explosion creates more nickel for each scenario. SN 1991T was considered superluminous and is grouped in this subclass (§ 5.2). We compare two models, W7DT (a Chandrasekhar mass late detonation that is very similar to W7 but includes additional nickel production nearer the surface) and HECD (a sub-Chandrasekhar mass helium detonation that is more massive and produces more nickel than HED8). These models produce brighter light curves (Fig. 12, *middle panel*), but the two superluminous explosion models do not differ dramatically, and it will be difficult to distinguish them based on the gamma-ray light curves alone. The result is that this type

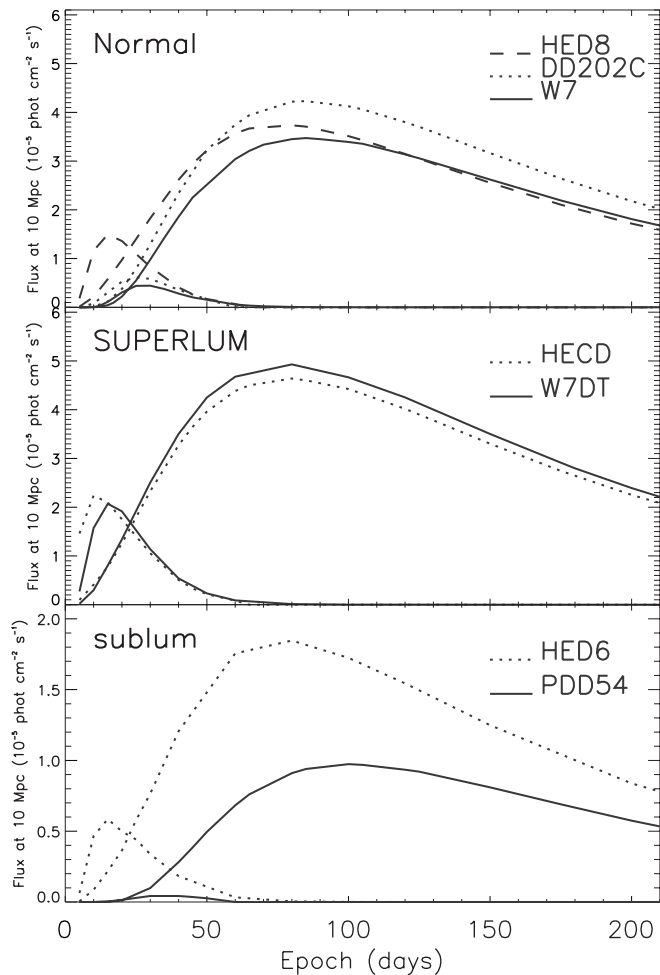


FIG. 12.—Line fluxes of the 812 and 847 keV lines for SN models representative of the three luminosity subclasses. The superluminous models (W7DT and HECD) have the brightest gamma-ray lines but are the most homogeneous, while the subluminous models (PDD54 and HED6) are faint but differ appreciably. The Chandrasekhar mass normally luminous models (W7 and DD202C) differ at late times as a result of their different nickel production, and the sub-Chandrasekhar mass model (HED8) differs early as a result of nickel produced very near the surface.

of explosion is detectable to large distances but is not distinguishable to a comparatively large distance.

The superluminous models are characterized by nickel near the surface of the ejecta. While this leads to 812 keV emission at earlier epochs than predicted for normally luminous SN Ia models, the 812 keV peak is much lower than suggested in HWK98 and Kumagai & Nomoto (1997). The largest deviations between past works and this current work occur in this “superluminous” type Ia subclass.

4.3. Subluminous SNe Ia

This subclass is the least promising for gamma-ray studies. SN 1986G was considered a slightly subluminous event and is best (although imperfectly) grouped in this subclass (§ 5.1). Subluminous events are less frequent than normally luminous SNe Ia and produce much fainter gamma-ray emission. For Chandrasekhar mass explosions, the nickel production is very low and is all concentrated near the center of the SN. This results in extremely faint gamma-ray emission. Sub-Chandrasekhar mass explosions also produce very little nickel but occur in lower mass objects, so the high escape fractions

⁷ Although we do not use this information, we mention that Li et al. (2000) assert that roughly 60% of SNe Ia are considered normally luminous, 20% subluminous, and 20% superluminous.

partially compensate for the lower nickel production. We compare two models, PDD54 (a Chandrasekhar mass pulsed delayed detonation) and HED6 (a very low mass helium detonation). Different subluminous models produce quite different light curves, but all are so faint that they will be difficult to detect (Fig. 12, *bottom panel*).

5. OBSERVED SNe Ia

In the last 25 years, there have been three SNe Ia that were close enough to warrant observations with gamma-ray telescopes.⁸ Although none of the three resulted in significant detections, papers have been written that infer the nickel production in each SN based on the observations. We revisit these three observations and discuss to what level they constrain the potential explosion mechanisms.

5.1. *SMM* Observations of SN 1986G

SN 1986G was first detected in Centaurus A on 1986 May 3 (Evans & McNaught 1986). It was discovered one week before maximum light and exhibited a relatively narrow luminosity peak. Its high $\Delta m_{15}(B)$ value led to its classification as a slightly subluminous SN (Hamuy et al. 1996). Heavy host galaxy extinction was suggested by both the photometric colors and strong Na D absorption. Although some papers have argued that the extinction was large enough to infer an absolute magnitude in the normal range (Cristiani et al. 1992), recent studies of the host galaxy extinction to SNe Ia maintain that SN 1986G was slightly subluminous (Phillips et al. 1999).

The Gamma-Ray Spectrometer on board *SMM* observed the SN with sensitivity that varied from 30% to full sensitivity during the entire epoch of cobalt decay. Matz & Share (1990) derived upper limits for the 847 and 1238 keV line emission from *SMM* spectra. They used escape fractions published by Gehrels et al. (1987) from a collection of parameterized SN Ia models to derive that the upper limits for the nickel production ranged from 0.36 to 0.41 M_{\odot} (assuming a distance of 3 Mpc to Centaurus A). This upper limit is marginally consistent with the $0.45 \pm 0.03 M_{\odot}$ ^{56}Ni production (scaling the distance from 3.3 ± 0.3 to 3.0 Mpc) derived from the nebular spectra (Ruiz-Lapuente & Lucy 1992).

Matz & Share (1990) quoted their results in terms of the ^{56}Ni production allowed by the observations. We do not reanalyze the *SMM* observations. Instead, we compare the average fluxes during the 1986 August 25–October 9 interval during which the *SMM* sensitivity was the largest. A review of the escape fractions from Gehrels et al. (1987) confirms that their range is in agreement with the simulations performed in this work. The *SMM* instrument had a ~ 80 keV FWHM at these energies and thus sampled a broad range of the continuum in addition to the two lines. However, for most of the epochs included in the composite *SMM* observation, the SN would have been expected to emit a relatively faint continuum. Thus, very little error is introduced by using tagged line photons and ignoring the instrument energy resolution for this SN.

In Figure 13 we compare light curves for five models with the light curves for the three models treated in Matz & Share (1990), in all cases setting the distance to be 3.3 Mpc. The three Matz & Share (1990) light curves assume the 3σ upper limit ^{56}Ni masses, while the other models use the published masses (as listed in Table 4). While only the 847 keV line emission is

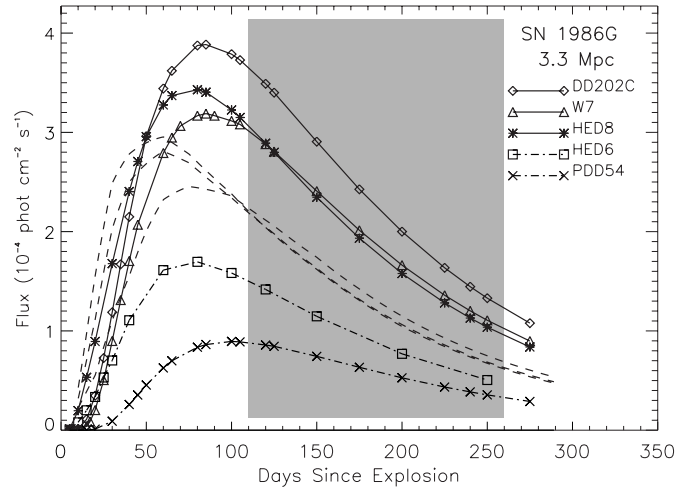


FIG. 13.—Five current simulations of 847 keV line emission from SN Ia models at 3.3 Mpc compared with 3σ upper limit light curves derived from *SMM* observations of SN 1986G (Matz & Share 1990). The three Matz & Share (1990) light curves are shown with dashed lines; the five current simulations are identified as shown. The epoch of maximum *SMM* angular response to SN 1986G is shaded. The normally luminous models appear too bright at the 3σ level, while the very subluminous models are acceptably faint.

shown in the figure, the upper limit ^{56}Ni masses were based on a joint 847–1238 keV line fit. The figure shows that the three normally luminous SN Ia models (DD202C, W7, and HED8) all produce too much 847 keV emission, while the very subluminous SN Ia models are faint enough to remain below the upper limits, especially for the low-nickel PDD54.

Note that all of these light curves assume the distance to Centaurus A to be 3.3 Mpc. Measures of this distance arrive at 3.1 ± 0.1 (Tonry & Schechter 1990) and 3.6 ± 0.2 Mpc (Jacoby et al. 1988), suggesting that slightly more ^{56}Ni production could be permissible. Thus, it appears that SN 1986G was tantalizingly close to being detected by *SMM*, and it would have been detected had it been a normally luminous or superluminous event rather than slightly subluminous. Nonetheless, the upper limit is consistent with the current understanding of SNe Ia and the simulation of gamma-ray escape from SN models.

5.2. *CGRO* COMPTEL and *OSSE* Observations of SN 1991T

SN 1991T was first detected in NGC 4527 on 1991 April 13 by S. Knight more than a week before maximum light (see Waagen et al. 1991). Its premaximum spectra featured iron peak elements instead of the intermediate-mass elements of normal SNe Ia, but, after peak, it was spectroscopically normal. The light curves were broad [$\Delta m_{15}(B)$ value of 0.94], leading to the suggestion that SN 1991T was a superluminous SN Ia and became a template slow SN Ia (although slower SNe exist). SN Ia models were produced explicitly to explain the optical observations of SN 1991T; we have included two of these models in this study (W7DT and HECD).

CGRO had just been launched (1 week before the discovery of SN 1991T), and months of calibrations and other testing had to be performed before the instruments on board *CGRO* could observe the SN. Observations were initiated on June 15, 67 days after the explosion (assuming that the SN was detected 3 days after the explosion), and continued in three viewing periods (3, 8, 11) until 190 days after the explosion (COMPTEL observed only viewing periods 3 and 11). There were two instruments on *CGRO* that were capable of detecting the 847 and 1238 keV

⁸ The subluminous SN Ia, SN 2003gs, was observed with the SPI instrument on the *INTEGRAL* satellite. The analysis of those observations has not been completed.

lines from the SN, the COMPTEL and OSSE instruments. Separate analyses were performed on the two sets of observations. Initially, COMPTEL reported only upper limits for the 847 and 1238 keV lines, arriving at 2σ upper limits for the 847 keV line of 3.0×10^{-5} and 3.2×10^{-5} photons $\text{cm}^{-2} \text{s}^{-1}$ for each viewing period (Lichti et al. 1994). A later, independent analysis suggested a combined 3.3σ detection (Morris et al. 1997). OSSE analysis derived only upper limits, reporting a 3σ upper limit of $(4.1\text{--}6.6) \times 10^{-5}$ photons $\text{cm}^{-2} \text{s}^{-1}$ for the 847 keV line during the first observation, based on a combined, simultaneous fit to the 847 and 1238 keV lines during all three epochs (Leising et al. 1995). When fitted separately, the formal fluxes are $(1.3 \pm 2.2, -0.2 \pm 3.2, 1.9 \pm 2.7) \times 10^{-5}$ photons $\text{cm}^{-2} \text{s}^{-1}$ for the 847 keV line for each of the three viewing periods (M. D. Leising 2004, private communication). We compare five models to the OSSE observations combined with each of the COMPTEL results (Fig. 14).

The uncertainty of the distance to NGC 4527 has made interpretation of the upper limits to the gamma-ray emission complicated. Using the distances to suggested neighbor galaxies yielded a range of distances from 10 to 17 Mpc. With such a range, astronomers could either largely reject the SN Ia models by the observed upper limits or find that almost all models were consistent (see Leising et al. 1995 for an explanation of the difficulties simultaneously explaining the optical and gamma-ray observations of SN 1991T). New studies have narrowed the distances to a range of 11.3–14.0 Mpc (Richtler et al. 2001; Gibson & Stetson 2001; Saha et al. 2001).⁹ For this work, we place NGC 4527 at 11.3 and 14.0 Mpc.

OSSE did not detect emission from SN 1991T, although VP3 was very near the peak of the simulated cobalt line peaks. Thus, those observations favor models that feature low gamma-ray fluxes. However, the modest sensitivity of the OSSE instrument limits the ability to discriminate between explosion scenarios.

The COMPTEL observations would, in principle, strengthen the ability to distinguish explosion scenarios. However, this is not (unambiguously) the case because the two separate analyses of the COMPTEL data arrived at dramatically different conclusions. The analysis by Lichti et al. (1994) detected no emission from SN 1991T and thus favors models that feature low gamma-ray fluxes. When combined with the OSSE observations, the COMPTEL upper limits further favor low gamma-ray flux models, at the level that the brighter models would be considered inconsistent (Leising et al. 1995). By contrast, the Morris et al. (1997) analysis measures fluxes brighter than predicted by any of the models. Using those fluxes, the highest flux models are favored, the more sensitive COMPTEL observations counteracting the OSSE upper limits.

The inability to reconcile these data sets severely limits the physics that can be derived from the observations (at least at the current level of understanding of SN Ia explosion physics). The OSSE observations do not reject any of the explosion scenarios if the larger NGC 4527 distance is used, and the COMPTEL observations are ambiguous.

5.3. CGRO COMPTEL Observations of SN 1998bu

SN 1998bu was discovered by M. Villi on 1998 May 9 (Villi et al. 1998) in M96 (NGC 3368), more than a week before

⁹ We note that the current range of distances, combined with extinction estimates, leads to the absolute magnitude of SN 1991T spanning the scatter of SNe Ia about the LWR (i.e., the 11.3 Mpc distance would make SN 1991T faint for its light-curve shape, while the 14 Mpc distance would make it slightly bright for its light-curve shape).

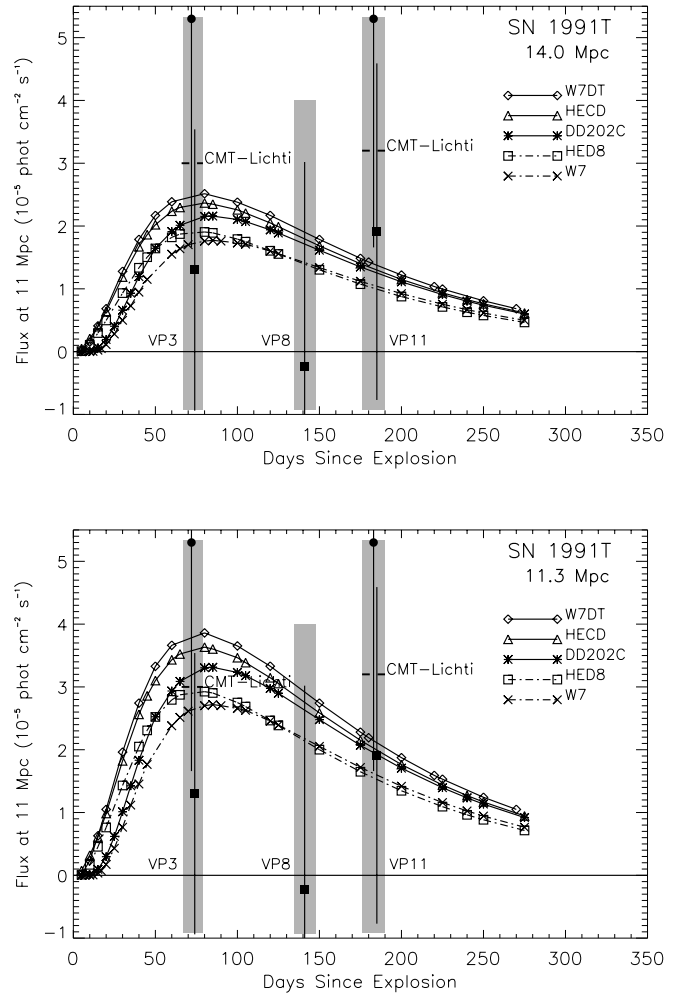


FIG. 14.—Five current simulations of 847 keV line emission from SN Ia models at two assumed distances compared with COMPTEL and OSSE observations of SN 1991T. The top panel shows the models at the larger distance of 14.0 Mpc, and the bottom panel shows the models at 11.3 Mpc. The five current simulations are identified as shown. The shaded regions show the three viewing periods, VP3, VP8 (OSSE only), and VP11. The OSSE data points (filled squares) and COMPTEL-Lichti (2σ upper limits; dashed lines) are fainter than the models, while the COMPTEL-Morris (filled circles) are brighter than the models (Lichti et al. 1994; Leising et al. 1995; Morris et al. 1997). The fluxes were all derived from joint 847/1238 keV line fits.

maximum light, affording *CGRO* a second opportunity to observe an SN Ia. This SN was determined to be a normally luminous SN [$\Delta m_{15}(B) = 1.02 \pm 0.04$; Jha et al. 1999]. Distance estimates have ranged from 9.6 ± 0.6 Mpc from planetary nebulae (Feldmeier et al. 1997) to 11.6 ± 0.9 Mpc from *Hubble Space Telescope* (*HST*) Cepheid period luminosity estimates (Tanvir et al. 1995). Subsequent *HST* Cepheid period luminosity estimates place M96 at 9.9–11.3 Mpc (Gibson & Stetson 2001; Gibson et al. 2000; Hjorth & Tanvir 1997), the range we use in this study. The *CGRO* team was able to begin observations at about maximum light. A total of 88 days of observing by both the COMPTEL and the OSSE instruments were devoted to SN 1998bu (spanning 17–136 days after the explosion), again resulting in two separate data sets. Neither instrument detected 847 or 1238 keV line emission. The OSSE instrument reported a 3σ upper limit for 3×10^{-5} photons $\text{cm}^{-2} \text{s}^{-1}$ for the 847 keV line based on a combined fit to the 847 and 1238 keV lines (Leising et al. 1999). When treated separately, the derived formal fluxes are $(1.2 \pm 1.4) \times 10^{-5}$

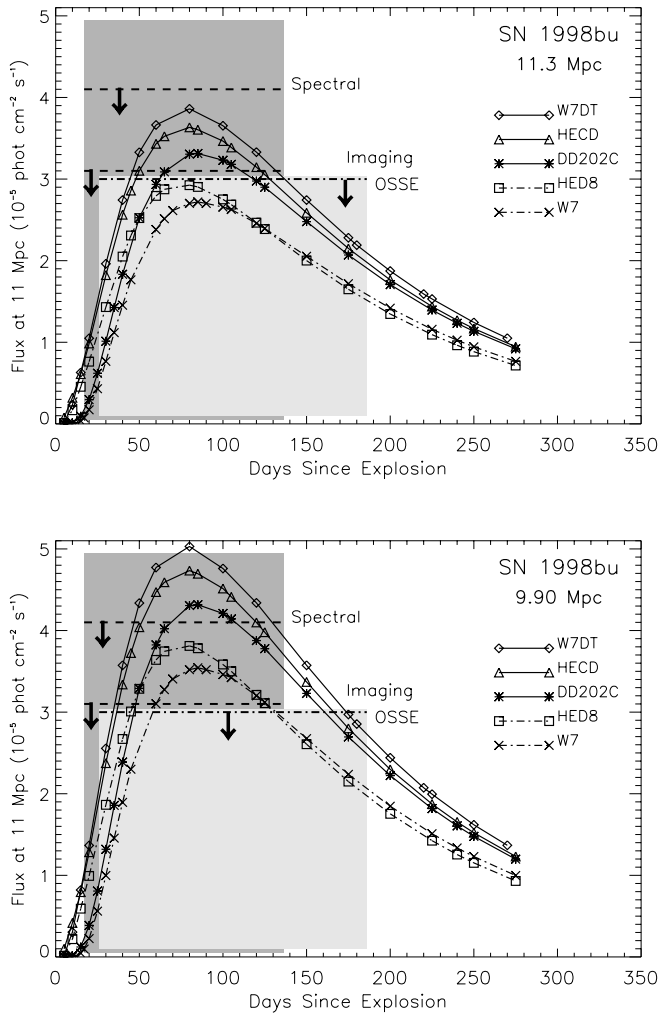


FIG. 15.—Five current simulations of 847 keV line emission from SN Ia models at two assumed distances compared with COMPTEL and OSSE observations of SN 1998bu. The top panel shows the models at the larger distance, 11.3 Mpc, and the bottom panel shows the models at 9.9 Mpc. The five current simulations are identified as shown. The light shaded region shows roughly the epoch of OSSE observations, while the dark shaded region shows roughly the epoch of COMPTEL observations. The two COMPTEL upper limits (Imaging and Spectral; *dashed lines*) are at the 2σ level (Georgii et al. 2002). The OSSE 3σ upper limits (*dot-dashed line*) are based on a joint 847/1238 keV line fit. Table 5 shows the probabilities of each model being consistent with the data at the two distances.

and $(-0.6 \pm 1.6) \times 10^{-5}$ photons $\text{cm}^{-2} \text{s}^{-1}$ for the 847 and 1238 keV lines (M. D. Leising 2004, private communication). The COMPTEL 2σ upper limits are 3.1×10^{-5} and 2.3×10^{-5} photons $\text{cm}^{-2} \text{s}^{-1}$, respectively (using the lower of the imaging and spectral analysis results for each line, from Georgii et al. 2002).

We first study the larger distance to NGC 3368. Comparison of the three normally luminous SN models with these upper limits finds that W7 and HED8 peak at or below the COMPTEL imaging upper limit for the 847 keV line and that average flux of DD202C is approximately equal to the COMPTEL imaging upper limit (Fig. 15). All three models are consistent with the combined OSSE and COMPTEL, 847 and 1238 keV data at a 10% probability, or better using the χ^2 test to the individual data points (Table 5). The superluminous SN models (HECD and W7DT) are brighter than the normally luminous models and are less likely to be as faint as the

TABLE 5
COMPARISONS OF SN Ia MODELS WITH SN 1998bu

Model Name	$F_{10 \text{ Mpc}}^{75 \text{ days}}$ ($10^{-5} \text{ cm}^{-2} \text{ s}^{-1}$)	Consistency at 9.9 Mpc (%)	Consistency at 11.3 Mpc (%)
W7.....	3.3	3.87	29.4
HED8.....	3.7	1.48	19.8
DD202C.....	4.1	0.40	11.5
W7DT.....	4.6	0.05	4.73
HECD.....	4.9	0.02	2.84

NOTE.—OSSE data from Leising et al. 1999, COMPTEL data from Georgii et al. 2002.

combined measurements. Considering that the optical observations favor a normally luminous SN Ia, the nondetection is consistent with expectations.

Assuming the shorter distance to NGC 3368, the upper limits become a great deal more constraining. Only W7 appears to be faint enough to rise above the 2% probability level for having neither instrument detect emission from the SN. The gamma-ray observations appear to favor a larger distance to NGC 3368.

Comparing these interpretations with Georgii et al. (2002), the conclusions are similar, but not identical. Principally, at the larger distance, that work only rejects the high ^{56}Ni producing models, while at the shorter distance that work rejects all normally luminous models. They use the light curves shown in Kumagai & Nomoto (1997) for HECD, W7DT, W7, and WDD2, which were high as discussed in § 4. The delayed detonation light curves from that work are very similar to the DD202C light curve shown in Figure 15. We note that Table 1 in that work shows average fluxes that correspond to their shorter distance of 9.6 Mpc, not the 11.3 Mpc shown in their Figure 6, and should thus be compared with our first column in Table 5. It is also worth noting that the *CGRO* observations spanned the epoch at which normally luminous models predict the brightest 847 and 1238 keV line emission. Thus, the non-detection is not likely to have been affected by delay in the *CGRO* observations.

6. CONCLUSIONS

In this paper we compare gamma-ray emission simulations from seven transport codes using a diverse set of SN Ia models. The spectra for three models (DD202C, W7, HED6) at explosion times ranging from 5 to over 200 days provide tests of these codes for a range of extreme conditions. This information allowed us to track down a number of errors in past results and correct for these errors. The results of HWK98 and Kumagai & Nomoto (1997) had the most dramatic errors, but their revised “current” codes now agree much better with our “unified” solution.

To the extent that one-dimensional SN Ia models closely approximate the physical SN explosion, observations can now be confidently compared with simulations. With current explosion scenarios and precise flux measurements, sub-Chandrasekhar mass models can be clearly distinguishable from Chandrasekhar mass models for normal and subluminous SNe Ia. However, with a suitably sensitive instrument, comparisons between line shapes, in addition to line fluxes, provide the best means to distinguish different explosion scenarios (HWK98).

Contrary to some of the past results, comparing to current data on SNe Ia finds that, for the subclass of each explosion,

theoretical gamma-ray line fluxes from one-dimensional models are consistent with the observations. However, bear in mind that the explosion scenarios shown are limited by the adequacy of one-dimensional modeling, and truly accurate comparisons will require three-dimensional explosions and transport calculations. In particular, clumping and global asymmetries will produce line profiles that differ from the profiles shown in this study. The wide range of line profiles possible with three-dimensional simulations and the resulting potential for confusion were partial motivation for this study.

Finally, recall that the inverse of calculating the gamma rays that escape the SN ejecta (producing the gamma-ray flux) is the energy that is deposited into the SN ejecta. The ability to simulate the optical/IR/UV light curves of SNe Ia depends on this deposition being accurately treated. This project does not directly address the energy deposition aspect of these simulations (and thus makes no claims), but errors in the decay rates and escape fraction may also lead to discrepancies in the energy deposition. Gamma-ray transport, which provides the

initial input for the emission of optical light, must be understood to model the optical light curves of SNe.

The authors would like to thank Peter Höflich for assistance in running his gamma-ray transport code, MC-GAMMA, and Mark Leising for providing OSSE results from SN 1991T and SN 1998bu.

This work was performed under the auspices of the US Department of Energy by Los Alamos National Laboratory, under contract W-7405-ENG-36, and by the National Science Foundation (CAREER grant AST 95-01634), with support from DOE SciDAC grant DE-FC02-01ER41176. L.-S. The acknowledges support from the DoE HENP Scientific Discovery through Advanced Computing Program. The research of J. I., E. B., and A. H. has been partially supported by the CIRIT and MCyT programs AYA2001-2360 and AYA2002-04094 and by the EU FEDER funds. A. H. is grateful to the IGSO program for a grant.

REFERENCES

- Ait-Ouamer, A. D., Kerrick, D. A., O'Neill, J. T., Tumer, T. O., Zych, D. A., & White, S. R. 1990, in Proc. 21st Int. Cosmic Ray Conf. (Adelaide), 183
- Ambwani, K., & Sutherland, P. 1988, *ApJ*, 325, 820
- Boggs, S. E. 2004, *ApJ*, submitted
- Boggs, S. E., & Jean, P. 2001, *A&A*, 376, 1126
- Brown, B. L., & Leventhal, M. 1987, *ApJ*, 319, 637
- Browne, E., & Firestone, R. B. 1987, in 8th Table of Radioactive Isotopes, ed. V. S. Shirley (New York: Wiley)
- Burrows, A., & The, L.-S. 1990, *ApJ*, 360, 626
- Bussard, R. W., Burrows, A., & The, L.-S. 1989, *ApJ*, 341, 401
- Chan, K.-W., & Lingenfelter, R. E. 1987, *ApJ*, 318, L51
- . 1993, *ApJ*, 405, 614
- Clayton, D. D., Colgate, S. A., & Fishman, G. J. 1969, *ApJ*, 155, 75
- Clayton, D. D., & The, L.-S. 1991, *ApJ*, 375, 221
- Cristiani, S., et al. 1992, *A&A*, 259, 63
- Evans, R., & McNaught, R. H. 1986, *IAU Circ.*, 4254, 3
- Feldmeier, J. J., Ciardullo, R., & Jacoby, G. H. 1997, *ApJ*, 479, 231
- Firestone, R. B. 1996, 8th Table of Isotopes, ed. V. S. Shirley (New York: Wiley)
- Freedman, W. L., et al. 2001, *ApJ*, 553, 47
- Gehrels, N., Leventhal, M., & MacCallum, C. J. 1987, *ApJ*, 322, 215
- Georgii, R., et al. 2002, *A&A*, 394, 517
- Gibson, B. K., & Stetson, P. B. 2001, *ApJ*, 547, L103
- Gibson, B. K., et al. 2000, *ApJ*, 529, 723
- Gómez-Gomar, J., Isern, J., & Jean, P. 1998, *MNRAS*, 295, 1
- Hamuy, M., Phillips, M. M., Suntzeff, N. B., Schommer, R. A., Maza, J., & Aviles, R. 1996, *AJ*, 112, 2391
- Harris, M., Teegarden, B. J., Cline, T. L., Gehrels, N., Palmer, D. M., Ramaty, R., & Seifert, H. 1998, *ApJ*, 501, L55
- Harrison, F. A., et al. 2003, *Proc. SPIE*, 4851, 345
- Hjorth, J., & Tanvir, N. R. 1997, *ApJ*, 482, 68
- Höflich, P. 2002, *NewA Rev.*, 46, 475
- Höflich, P., & Khokhlov, A. 1996, *ApJ*, 457, 500
- Höflich, P., Khokhlov, A., & Müller, E. 1992, *A&A*, 259, 549
- Höflich, P., Khokhlov, A., & Wheeler, J. C. 1995, *ApJ*, 444, 831
- Höflich, P., & Wheeler, J. C. 2004, *ApJ*, 605, 573
- Höflich, P., Wheeler, J. C., & Khokhlov, A. 1998a, *ApJ*, 492, 228 (HWK98)
- Höflich, P., Wheeler, J. C., & Thielemann, F.-K. 1998b, *ApJ*, 495, 617
- Hungerford, A. L., Fryer, C. L., & Warren, M. S. 2003, *ApJ*, 594, 390
- Isern, J., Gómez-Gomar, J., & Bravo, E. 1996, *Mem. Soc. Astron. Italiana*, 67, 101
- Isern, J., Gómez-Gomar, J., Bravo, E., & Jean, P. 1997, in Proc. 2nd *INTEGRAL* Workshop, ed. C. Winkler, J.-L. Courvoisier, & Ph. Durouchoux (Noordwijk: ESA), 89
- Iwabuchi, K., & Kumagai, S. 2001, *PASJ*, 53, 669
- Jacoby, G. H., Ciardullo, R., & Ford, H. C. 1988, in ASP Conf. Ser. 4, The Extragalactic Distance Scale, ed. S. van den Bergh & C. J. Pritchett (San Francisco: ASP), 42
- Jha, S., et al. 1999, *ApJS*, 125, 73
- Junde, H. 1999, *Nucl. Data Sheets*, 86, 315
- Kazaryan, S. M., Lupenko, V. G., Nazarova, I. N., Ryumin, P. S., Sukhanov, P. V., & Titenkov, F. A. 1990, in Proc. 21st Int. Cosmic Ray Conf. (Adelaide), 187
- Kinzer, R. L., et al. 2001, *ApJ*, 559, 282
- Kumagai, S., Iwabuchi, K., & Nomoto, K. 1999, in Proceedings of Astronomy with Radioactivities III, ed. R. Diehl & D. Hartmann (MPE Rep. 274; Garching: MPE), 181
- Kumagai, S., & Nomoto, K. 1997, in Thermonuclear Supernovae, ed. P. Ruiz-Lapuente, R. Canal, & J. Isern (NATO ASI Ser. C, 486; Dordrecht: Kluwer), 515
- Kurfess, J. D., et al. 1992, *ApJ*, 399, L137
- Lederer, C. M., Hollander, J. M., & Perlman, I. 1967, 6th Table of Isotopes (New York: Wiley)
- Lederer, C. M., & Shirley, V. S. 1978, 7th Table of Isotopes (New York: Wiley)
- Leising, M. D., The, L.-S., Höflich, P., Kurfess, J. D., & Matz, S. 1999, *BAAS*, 31, 703
- Leising, M. D., et al. 1995, *ApJ*, 450, 805
- Li, W. D., Filippenko, A. V., Riess, A. G., Treffers, R. R., Hu, J. Y., & Qiu, Y. L. 2000, in AIP Conf. Proc. 522, Cosmic Explosions, ed. S. S. Holt & W. W. Zhang (New York: AIP), 91
- Lichti, G. G., et al. 1994, *A&A*, 292, 569
- Livio, M. 2001, in Supernovae and Gamma-Ray Bursts: The Greatest Explosions since the Big Bang, ed. M. Livio, N. Panagia, & K. Sahu (Cambridge: Cambridge Univ. Press), 334
- Mahoney, W. A., Varnell, L. S., Jacobson, A. S., Ling, J. C., Radocinski, R. G., & Wheaton, W. A. 1988, *ApJ*, 334, L81
- Matz, S. M., & Share, G. H. 1990, *ApJ*, 362, 235
- Milne, P. A., Kroeger, D., Kurfess, J. D., & The, L.-S. 2002, *NewA Rev.*, 46, 617
- Milne, P. A., The, L.-S., & Kroeger, D. 2000, in Proc. 2nd Chicago Meeting on Thermonuclear Explosions, ed. J. Niemeyer, in press
- Milne, P. A., The, L.-S., & Leising, M. D. 1999, *ApJS*, 124, 503
- Mochizuki, Y., Takahashi, K., Janka, H.-Th., Hillebrandt, W., & Diehl, R. 1999, *A&A*, 346, 831
- Morris, D. J., et al. 1997, in AIP Conf. Proc. 410, Proc. 4th Compton Symp., ed. C. D. Dermer, M. S. Strickman, & J. D. Kurfess (New York: AIP), 1084
- Müller, E., Höflich, P., & Khokhlov, A. 1991, *A&A*, 249, L1
- Nomoto, K., Thielemann, F.-K., & Yokoi, K. 1984, *ApJ*, 286, 644
- Ore, A., & Powell, J. 1949, *Phys. Rev.*, 75, 1696
- Perlmutter, S., et al. 1997, *ApJ*, 483, 565
- Phillips, M. M., Lira, P., Suntzeff, N. B., Schommer, R. A., Hamuy, M., & Maza, J. 1999, *AJ*, 118, 1766
- Pinto, P. A., & Eastman, R. 2000a, *ApJ*, 530, 744
- . 2000b, *ApJ*, 530, 757
- Pinto, P. A., Eastman, R., & Rogers, T. 2001, *ApJ*, 551, 231
- Pinto, P. A., & Woosley, S. 1988, *Nature*, 333, 534
- Raeseide, D. E. 1976, *Phys. Med. Bio.*, 21, 181
- Rester, A. C., Coldwell, R. L., Dunnam, F. E., Eichhorn, G., Trombka, J. I., Starr, R., & Lasche, G. P. 1989, *ApJ*, 342, L71

- Richtler, T., Jensen, J. B., Tonry, J., Barris, B., & Drenkhahn, G. 2001, *A&A*, 368, 391
- Riess, A. G., et al. 1998, *AJ*, 116, 1009
- Ruiz-Lapuente, P., & Lucy, L. B. 1992, *ApJ*, 400, 127
- Saha, A., Sandage, A., Thim, F., Labhardt, L., Tammann, G. A., Christensen, J., Panagia, N., & Macchetto, F. D. 2001, *ApJ*, 551, 973
- Shigeyama, T., Kumagai, S., Yamaoka, H., Nomoto, K., & Thielemann, F.-K. 1993, *A&AS*, 97, 223
- Tanvir, N. R., Shanks, T., Ferguson, H. C., & Robinson, D. R. T. 1995, *Nature*, 377, 27
- Teegarden, B. J., Barthelmy, S. D., Gehrels, N., Tueller, J., & Leventhal, M. 1989, *Nature*, 339, 122
- The, L.-S., Bridgman, W., & Clayton, D. D. 1994, *ApJS*, 93, 531
- The, L.-S., Burrows, A., & Bussard, R. 1990, *ApJ*, 352, 731
- The, L.-S., Leising, M. D., & Clayton, D. D. 1993, *ApJ*, 403, 32
- Tonry, J. L., & Schechter, P. L. 1990, *AJ*, 100, 1794
- Tueller, J., Barthelmy, S., Gehrels, N., Teegarden, B. J., Leventhal, M., & MacCallum, C. J. 1990, *ApJ*, 351, L41
- Villi, M., Nakano, S., Aoki, M., Skiff, B. A., & Hanzl, D. 1998, *IAU Circ.*, 6899, 1
- Waagen, E., et al. 1991, *IAU Circ.*, 5239, 1
- Yamaoka, H., Nomoto, K., Shigeyama, T., & Thielemann, F.-K. 1992, *ApJ*, 393, L55